

# Development of an Ultra Wide-Band Antenna System for Automotive Applications

Master Thesis

Philipp Franz Freidl

---

Institute of Microwave and Photonic Engineering,  
Graz University of Technology



in cooperation with:  
Maxim Integrated



Supervisors: Prof. Dr. Erich Leitgeb, TU Graz  
Dr. Ivan Russo, TU Graz  
Dr. Thomas Gigl, Maxim Integrated

Graz, February 2013

## EIDESSTATTLICHE ERKLÄRUNG

Ich erkläre an Eides statt, dass ich die vorliegende Arbeit selbstständig verfasst, andere als die angegebenen Quellen/Hilfsmittel nicht benutzt und die den benutzten Quellen wörtlich und inhaltlich entnommenen Stellen als solche kenntlich gemacht habe.

Graz, am Monday 18<sup>th</sup> February, 2013

.....  
(Unterschrift)

Englische Fassung:

## STATUTORY DECLARATION

I declare that I have authored this thesis independently, that I have not used other than the declared sources / resources and that I have explicitly marked all material which has been quoted either literally or by content from the used sources.

Monday 18<sup>th</sup> February, 2013

.....  
(signature)

# Abstract

Wireless communication systems are nowadays widely used in many automotive applications. With the release of the Ultra Wide-Band in 2002, a low-power channel has been made available, which ensures a robust communication and ranging capabilities which are key features of such systems. However, the design of appropriate antennas has become a key challenge in the system design.

This thesis aims at designing antennas for the stationary (on-car) part of an automotive communication system between the car and a hand-held device (key). To support a simple and miniaturized linearly polarized hand-held antenna system, the stationary broadband (3–5 GHz) antennas are circularly polarized.

The first part of the thesis analyzes existing antenna designs which offer a circularly polarized transmitted wave over a broad frequency range. The second part describes the adaptation of two promising antenna designs with different radiation characteristics and feeding techniques to the given requirements.

# Kurzfassung

Drahtlose Kommunikation spielt heutzutage in automobilen Kommunikationssystemen eine immer größer werdende Rolle. Mit der Ultra-Breitband-Technologie, der im Jahr 2002 ein Frequenzbereich zur Nutzung mit kleinen Sendeleistungen zugewiesen wurde, kann ein robuster Kanal für breitbandige Pulse konzipiert werden. Die Konstruktion von Ultra-Breitband-Antennen wird daher zu einem Schwerpunkt der Systementwicklung.

Das Ziel der Diplomarbeit ist der Entwurf von Antennen für den stationären Teil des Kommunikationssystems zwischen dem Auto und dem mobilen Empfänger (Schlüssel). Um eine einfache Antennenstruktur im Empfänger zu ermöglichen, werden die stationären Antennen für eine zirkular polarisierte Abstrahlung entworfen.

Im ersten Teil der Diplomarbeit werden bereits veröffentlichte Antennen analysiert. Im zweiten Teil, werden zwei zirkular polarisierte Antennen konstruiert und ihre Charakteristiken im Hinblick auf die vorgegebenen Anforderungen ausgewertet.

# Acknowledgments

I would like to offer my gratitudes to “Maxim Integrated”, represented by *Dr. Gerhard Schultes*, which not only provided the initial idea and the fundings for this thesis, but also offered me an valuable supervision through *Dr. Thomas Gigl*.

For the academical supervision I would like to thank the Institute of Microwave and Photonic Engineering, especially *Prof. Dr. Erich Leitgeb* and *Dr. Ivan Russo*, who guided me through the theoretical and practical challenges of this project, and helped with word and deed if needed.

# Contents

<b>1</b>	<b>Introduction</b>	<b>1</b>
1.1	Motivation . . . . .	1
1.2	Requirements . . . . .	1
1.3	Structure of the Thesis . . . . .	1
<b>2</b>	<b>Antenna Fundamentals</b>	<b>2</b>
2.1	Radiation Intensity . . . . .	2
2.2	Input Impedance . . . . .	3
2.3	Directivity . . . . .	3
2.4	Efficiency . . . . .	3
2.5	Gain . . . . .	4
2.6	Beamwidth . . . . .	4
2.7	Radiation Lobes . . . . .	5
2.8	Polarization . . . . .	5
2.8.1	Linear Polarization . . . . .	5
2.8.2	Circular Polarization . . . . .	6
2.8.3	Elliptical Polarization . . . . .	6
2.9	Axial Ratio . . . . .	6
2.10	Bandwidth . . . . .	6
2.11	UWB Parameters . . . . .	8
2.11.1	Peak Value of the Envelope . . . . .	8
2.11.2	Width of the Envelope . . . . .	8
2.11.3	Ringing . . . . .	8
2.11.4	Group Delay . . . . .	9
<b>3</b>	<b>Evaluation of Dual- and Circular-Polarized Broadband Antenna Solutions</b>	<b>10</b>
3.1	Coordinate System . . . . .	10
3.2	Coplanar Waveguide-Fed Square Slot Antenna . . . . .	11
3.2.1	Geometry . . . . .	11
3.2.2	Antenna Characteristics . . . . .	12
3.3	L-shaped Probe and L-shaped Wide-Slot Antenna . . . . .	14
3.3.1	Geometry . . . . .	14
3.3.2	Antenna Characteristics . . . . .	15
3.4	Slot/Strip Loop Antenna . . . . .	17
3.4.1	Geometry . . . . .	17
3.4.2	Antenna Characteristics . . . . .	17
3.5	Circularly Fed Patch Antenna . . . . .	20
3.5.1	Geometry . . . . .	20
3.5.2	Antenna Characteristics . . . . .	21
3.6	Antipodal Tapered Slot Antenna . . . . .	23
3.6.1	Geometry . . . . .	23
3.6.2	Antenna Characteristics . . . . .	23
3.7	Comparison and Summary of the analyzed Antennas . . . . .	26

<b>4</b>	<b>Implementation of the Dual-Polarized Patch Antenna</b>	<b>28</b>
4.1	Design Elements . . . . .	28
4.1.1	Patch . . . . .	28
4.1.2	Feeding Structure . . . . .	31
4.1.3	Reflector . . . . .	32
4.2	Parametric analysis of the design elements . . . . .	32
4.2.1	Patch Parameterization . . . . .	32
4.2.2	Feeding Structure Parameterization . . . . .	34
4.2.3	Reflector Parameterization . . . . .	36
4.3	Implementation . . . . .	37
4.3.1	Input Characteristics . . . . .	38
4.3.2	Radiation Patterns . . . . .	38
4.3.3	UWB Characteristics . . . . .	41
<b>5</b>	<b>Implementation of the Antipodal Tapered- Slot Antenna</b>	<b>42</b>
5.1	Design Elements . . . . .	42
5.1.1	Coplanar Waveguide . . . . .	43
5.1.2	Substrate Integrated Waveguide . . . . .	44
5.1.3	Transition . . . . .	44
5.1.4	Tapered Slot . . . . .	45
5.1.5	Dielectric Rod . . . . .	45
5.2	Parametric Analysis of the Design Elements . . . . .	46
5.2.1	Coplanar Waveguide Parameterizations . . . . .	46
5.2.2	Substrate Integrated Waveguide Parameterizations . . . . .	46
5.2.3	Transition Parameterizations . . . . .	47
5.2.4	Tapered Slot Parameterizations . . . . .	48
5.2.5	Dielectric Rod Parameterizations . . . . .	49
5.3	Implementation . . . . .	51
5.3.1	Input Characteristics . . . . .	51
5.3.2	Radiation Patterns . . . . .	52
5.3.3	UWB Characteristics . . . . .	54
<b>6</b>	<b>Conclusion and Prospects</b>	<b>56</b>
6.1	Results . . . . .	56
6.2	Future Work . . . . .	57
	<b>List of Figures</b>	<b>58</b>
	<b>List of Tables</b>	<b>60</b>
	<b>Acronyms and Abbreviations</b>	<b>61</b>
	<b>Bibliography</b>	<b>62</b>

# 1 Introduction

The scope of this thesis is to develop some antenna designs for the on-car part of a ultra wide-band (UWB) key-less entry communication system according to the requirements given in Section 1.2. The final designs will be prototyped and measured in an anechoic chamber.

In this chapter the motivation of the project, as well as its requirements and the structure of the whole thesis are described.

## 1.1 Motivation

Wireless communication systems are nowadays widely used in many automotive applications. With the release of the Ultra-Wide Band in 2002 [1], a low-power communication channel with a frequency range from 3 GHz to 9 GHz has been made available for the commercial usage.

The possibility of using a broad frequency range and therefore broadband pulses for communicating between the stationary (on-car) and the mobile (key) component, allows the possibility of accurate and reliable locating the key around a specific entry area around the car.

## 1.2 Requirements

Frequency Range	3 - 5 GHz
Center Frequency	4 GHz
Minimum Bandwidth	500 MHz
Geometry	Planar
Polarization	circular
Antenna Pattern	wide main beam width

**Table 1.1:** Basic requirements for the antennas

A minimum bandwidth of 500 MHz at a center frequency of 4 GHz is required. For an easy installation on the car, a planar and small-sized geometry is necessary. Since the position of the receiving antenna cannot be predicted, a circular polarization with an axial ratio close to 1 is needed. To cover the entrance area of the car, a wide main beam aperture is required.

## 1.3 Structure of the Thesis

The first part of the thesis defines and describes various antenna parameters which are used to evaluate the performance of the antenna designs later on. The second part analyzes existing antenna designs which offer a circularly or dual polarized transmitted wave over a broad frequency range. The third part describes the adaptation of two promising antenna designs, with different radiation characteristics and feeding techniques to the given requirements. In the fourth part, prototypes of the final antenna designs are built and their characteristics are experimentally evaluated. The last part sums up the outcomes of the thesis and gives an outlook on the upcoming work on the project.

## 2 Antenna Fundamentals

In this chapter, antenna parameters, which will be used later on, and their definitions are explained.

### 2.1 Radiation Intensity

The radiation density is the propagating power density associated with electromagnetic field in the far-field region of an antenna.

The average power density itself can be described by the average Poynting vector  $\mathbf{W}_{av}$  (curly symbols are instantaneous fields and quantities) [2]:

$$\mathcal{W} = \mathcal{E} \times \mathcal{H} \quad (2.1)$$

$$\mathbf{W}_{av} = [\mathcal{W}(x, y, z; t)]_{av} = \frac{1}{2} \Re[\mathbf{E} \times \mathbf{H}^*] \quad (2.2)$$

$\mathcal{W}$  = instantaneous Poynting vector [ $\frac{\text{W}}{\text{m}^2}$ ]

$\mathcal{E}$  = instantaneous electric-field intensity [ $\frac{\text{V}}{\text{m}}$ ]

$\mathcal{H}$  = instantaneous magnetic-field intensity [ $\frac{\text{A}}{\text{m}}$ ]

For a given direction, the radiation intensity is defined as “the power radiated from an antenna per unit solid angle” [3]. The radiation intensity is a far-field parameter and can be obtained by multiplying the radiation density with the square of the distance. Also, the radiation density is related to the far-zone electrical field [2]:

$$U = r^2 W_{rad} \quad (2.3)$$

$$U(\theta, \phi) = \frac{r^2}{\eta} |\mathbf{E}(r, \theta, \phi)|^2 \quad (2.4)$$

$U$  = radiation intensity [ $\frac{\text{W}}{\text{unitsolidangle}}$ ]

$W_{rad}$  = radiation density [ $\frac{\text{W}}{\text{m}^2}$ ]

$\mathbf{E}(r, \theta, \phi)$  = far-zone electric-field intensity of the antenna

$\eta$  = intrinsic impedance of the medium ( $\eta_0 = \sqrt{\frac{\mu_0}{\epsilon_0}} = 276.8\Omega$ )

The total radiated power  $P_{rad}$  can be obtained by integrating the radiation intensity over a closed surface ( $\Omega$ ) around the antenna (Equation 2.5) [2].

$$P_{rad} = \oint_{\Omega} U \, d\Omega = \int_0^{2\pi} \int_0^{\pi} U \sin(\theta) \, d\theta \, d\phi \quad (2.5)$$

For an isotropic source with of which the radiation intensity  $U_0$  is constant with the angles  $\theta$  and  $\phi$ , the radiated power can be computed in Equation 2.6.

$$P_{rad0} = \oint_{\Omega} U_0 \, d\Omega = U_0 \oint_{\Omega} d\Omega = 4\pi U_0 \quad (2.6)$$

## 2.2 Input Impedance

The input impedance is defined as “the impedance presented by an antenna at its terminals”. [3]

This impedance can be obtained by the ratio of the voltage to current at the antenna terminals (Figure 2.1a). [2]

$$Z_A = R_A + jX_A; R_A = R_r + R_L \quad (2.7)$$

$Z_A$  antenna impedance at terminals a-b [ $\Omega$ ]

$R_A$  antenna resistance at terminals a-b [ $\Omega$ ]

$R_r$  radiation resistance of an antenna [ $\Omega$ ]

$R_L$  loss resistance of an antenna [ $\Omega$ ]

$X_A$  antenna reactance terminals a-b [ $\Omega$ ]

## 2.3 Directivity

The directivity of an antenna is “the ratio of the radiation intensity in a given direction from the antenna to the radiation intensity averaged over all directions. The average radiation intensity is equal to the total power radiated by the antenna divided by (the maximum steradian angle)  $4\pi$ . If the direction is not specified, the direction of maximum radiation intensity is implied” [3]. The general definition of the directivity is presented in Equation 2.8, while the maximum directivity is given in Equation 2.9.

$$D(\theta, \phi) = \frac{4\pi U(\theta, \phi)}{P_{rad}} = \frac{U}{U_0} \quad (2.8)$$

$$D_{max} = D_0 = \frac{U|_{max}}{U_0} = \frac{U_{max}}{U_0} = \frac{4\pi U_{max}}{P_{rad}} \quad (2.9)$$

$U_0$  reference radiation intensity of an isotropic radiator

Looking again at an isotropic source,  $U_{max}$  and  $U_0$  are equal to each other, which leads to a constant directivity of  $D = D_0 = 1$ .

For sources with orthogonal polarization components ( $E_\theta$  and  $E_\phi$ ) the directivity can be separated into two partial directivities  $D_\theta$  and  $D_\phi$  [2]

$$D_0 = D_\theta + D_\phi \quad (2.10)$$

$$D_\theta = \frac{4\pi U_\theta}{(P_{rad})_\theta + (P_{rad})_\phi} \quad (2.11)$$

$$D_\phi = \frac{4\pi U_\phi}{(P_{rad})_\theta + (P_{rad})_\phi} \quad (2.12)$$

## 2.4 Efficiency

Every antenna is characterized by some efficiency factors, which can be defined in terms of different phenomena such as the input reflection coefficient ( $\Gamma$ ) and dielectric and conductive loss currents ( $i_d$  and  $i_c$ ) in Figure 2.1b [2].

$\eta_r$  reflection efficiency describes the losses at the input terminals due to mismatch between the antenna and the transmission line (Equation 2.13);

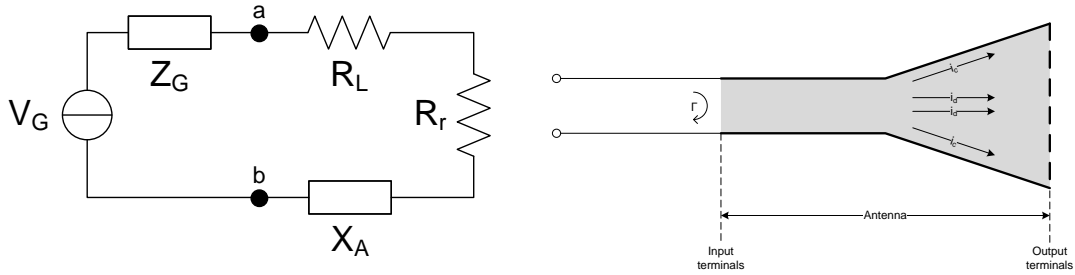
$$\eta_{cd} = \left( \frac{R_r}{R_r + R_L} \right) \quad (2.13)$$

$\eta_{cd}$  radiation efficiency describes the conductive and dielectric losses ( $I^2R$ ) within the antenna structure (Equation 2.14).

$$\eta_r = (1 - |\Gamma|^2); \Gamma = \left( \frac{Z_g - Z_{in}}{Z_g + Z_{in}} \right) \quad (2.14)$$

$\eta_0$  is the total efficiency of an antenna and varies between 0 and 1.

$$\eta_0 = \eta_{cd}\eta_r \quad (2.15)$$



(a) Thevenin equivalent circuit

(b) reference terminals and losses of an antenna

**Figure 2.1:** Thevenin equivalent circuit and reference terminals and losses of an antenna [2]

## 2.5 Gain

The gain  $G(\theta, \phi)$  of an antenna is a useful measure to determine its performance. It is closely related to the directivity  $D(\theta, \phi)$ , which is only describing the directional properties of the antenna but does not include the efficiency.

The normal gain  $G(\theta, \phi)$  takes only conductive and dielectric losses into account, while the realized gain (or absolute gain)  $G_r(\theta, \phi)$  considers the whole system losses [2].

$$G(\theta, \phi) = \eta_{cd}D(\theta, \phi) \quad (2.16)$$

$$G_r(\theta, \phi) = \eta_r\eta_{cd}D(\theta, \phi) = \eta_0D(\theta, \phi) \quad (2.17)$$

## 2.6 Beamwidth

The main beam aperture (or half-power beamwidth, HPBW) is the angle between the two directions where the radiation dropped to the half compared to the maximum radiation (Figure 2.2) [2].

Besides the half-power beamwidth, a first-null beamwidth (FNBW) which measures the separation angle between the first nulls of the pattern, can be defined [2]

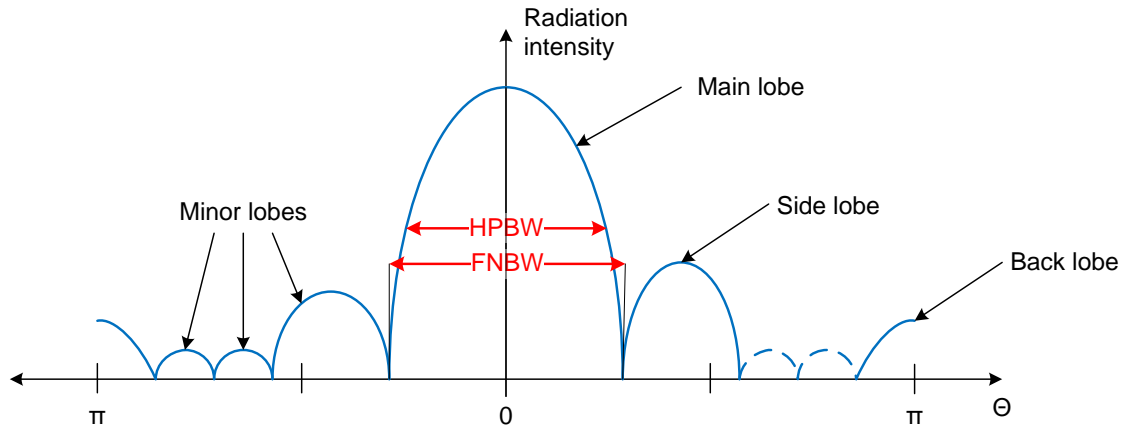


Figure 2.2: Main beam aperture and radiation lobes of an antenna pattern [2]

## 2.7 Radiation Lobes

The radiation pattern of an antenna (Figure 2.2) can be divided in several lobes (areas with a local maxima bounded by regions of relative weak intensity). These lobes can be sub-classified into [2]:

**main lobe** “the lobe containing the direction maximum radiation (also referred as major lobe)”,

**minor lobe** “any radiation lobe except a main lobe”,

**side lobe** “a radiation lobe in any direction other than that of the major lobe”,

**back lobe** “a radiation lobe whose axis makes an angle of approximately 180 degrees with respect to the beam axis of an antenna” [3].

## 2.8 Polarization

The polarization of a radiated wave is defined as “that property of an electromagnetic wave describing the time-varying direction and relative magnitude of the electric-field vector; specifically, the Figure traced as a function of time by the extremity of the vector at a fixed location in space, and the sense in which it is traced, as observed along the direction of propagation.” Therefore, polarization can be represented by the curve which is traced by the end point of the arrow which is representing the instantaneous electric field (Figure 2.3a). [2]

For different  $\mathcal{E}_\theta(r; t)$  and  $\mathcal{E}_\phi(r; t)$  3 different main types of polarization can be defined:

### 2.8.1 Linear Polarization

The tip of the field vector of a linear polarized wave is oriented on the same straight line for every instant of time (Figure 2.3c). This is accomplished by having either only one component, or two orthogonal components which are in phase or have a phase-shift of a multiple of  $180^\circ$  [2].

$$\Delta\phi = \phi_\theta - \phi_\phi = n\pi, n = 0, 1, 2, 3, \dots \quad (2.18)$$

## 2.8.2 Circular Polarization

The tip of the field vector of a circularly polarized wave travels along a circle (Figure 2.3d). To achieve this, the two orthogonal components of the electric field must have the same magnitude, and a phase shift of an odd multiple of  $90^\circ$ .

$$|\mathcal{E}_\theta| = |\mathcal{E}_\phi| \rightarrow E_{\theta,0} = E_{\phi,0} \quad (2.19)$$

$$\Delta\phi = \phi_\theta - \phi_\phi = \pm\left(\frac{1}{2} + n\right)\pi, n = 0, 1, 2, 3, \dots \quad (2.20)$$

According to [2]: “The sense of the rotation of the instantaneous electric-field vector is determined by rotating the phase-leading component toward the phase-lagging component and observing the field rotation as the wave is viewed as it travels away from the observer. If the rotation is clockwise, the wave is right-hand (or clockwise) circularly polarized (RHCP); if the rotation is counterclockwise, the wave is left-hand (or counterclockwise) circularly polarized (LHCP). The rotation of the phase-leading component toward the phase lagging component should be done along the angular separation between the two components that is less than  $180^\circ$ . Phases equal to or greater than  $0^\circ$  and less than  $180^\circ$  should be considered as leading whereas those equal to or greater than  $180^\circ$  and less than  $360^\circ$  should be considered lagging.”

## 2.8.3 Elliptical Polarization

The tip of the field vector of an elliptically polarized wave traces an elliptical curve (Figure 2.3b). As this is the most general case of polarization, the elliptical polarization can be achieved by two orthogonal field components with different magnitude and a phase shift different to  $0^\circ$  (which would lead to a linear polarization) or a multiple of  $180^\circ$ , or the same magnitude and a phase shift different to an odd multiple of  $90^\circ$  [2].

The sense of polarization for elliptical polarization is determined in the same way as it is done for circular polarization (Section 2.8.2)

## 2.9 Axial Ratio

In any elliptical polarized wave, two orthogonal components of the electrical field exist (Figure 2.3b). The axial ratio defines the ratio between the major component and the minor component (Equation 2.21). For a circularly polarized (CP) wave, those two components have an equal amplitude, and therefore an axial ration of 1.

$$AR = \frac{E_{major,0}}{E_{minor,0}} \quad (2.21)$$

## 2.10 Bandwidth

The bandwidth of an antenna is defined as “the range of frequencies within which the performance of the antenna, with respect to some characteristics, conforms to a specified standard [3].”

The bandwidth can be considered as the range of frequencies around a center frequency, where the variation of the respected characteristics (such as input impedance, patterns, beamwidth, beam direction, gain...) is within an acceptable range (Figure 2.4).

Since the respected antenna characteristics do not necessarily vary in the same manner. Therefore there is no unique bandwidth. The set of characteristics which is used for the characterization of the

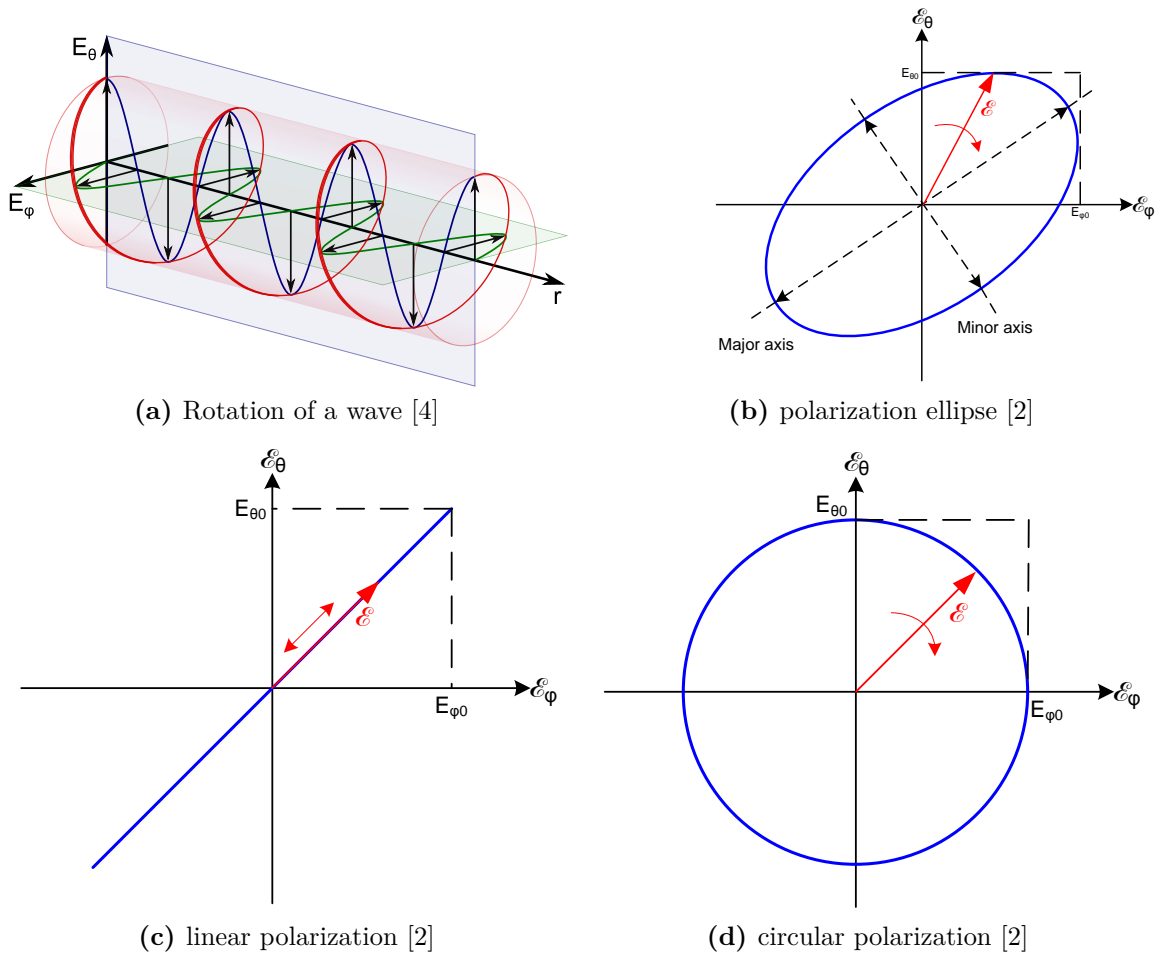


**Figure 2.3:** Rotation of an electromagnetic wave and its polarization ellipse

bandwidth is chosen in each case to meet the needs of the application. Usually there is a distinction between pattern and input impedance variations (*pattern bandwidth* and *impedance bandwidth*) [2].

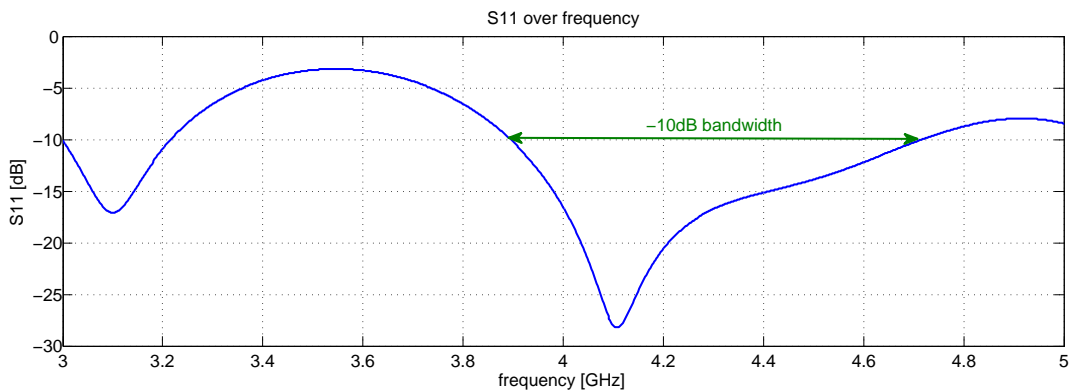


**Figure 2.4:** Input impedance bandwidth of a tapered slot antenna

## 2.11 UWB Parameters

Different to common narrow-band antennas, ultrawide band antennas require additional properties and representations do validate their suitability for different applications. Using linear system theory, the characteristics of an antenna can be completely described in the time-domain impulse response  $\mathbf{h}(t, \theta_{Tx}, \phi_{Tx})$  or the frequency-domain transfer function  $\mathbf{H}(f, \theta_{Tx}, \phi_{Tx})$

Using the Hilbert transform  $\mathcal{H}$ , the analytical impulse response  $h^+(t)$  can be calculated:

$$h^+(t) = (h(t) + j\mathcal{H}\{h(t)\}) \quad (2.22)$$

The envelope  $|h^+(t)|$  of the analytical impulse response gives an overview of the distribution of the transmitted energy over the time in a given direction [5].

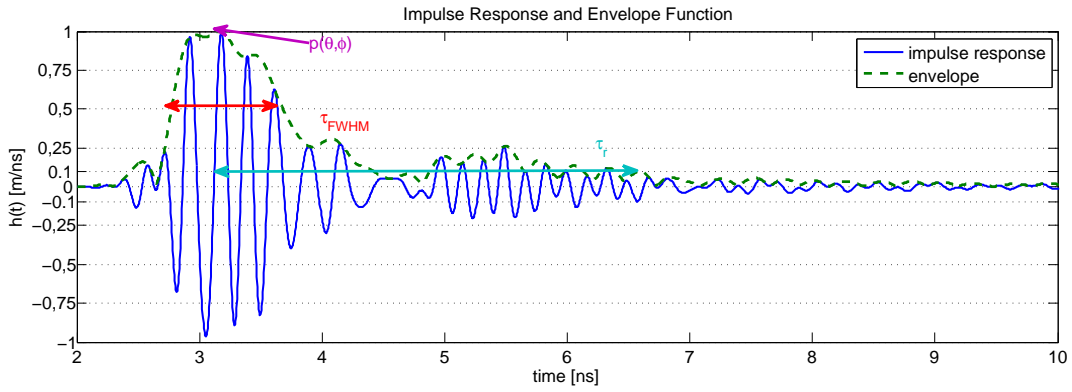


**Figure 2.5:** Impulse response and its envelope of a tapered slot antenna

### 2.11.1 Peak Value of the Envelope

The peak value of the envelope  $p(\theta, \phi)$  indicates the maximal value of the envelope of the analytical impulse response (Figure 2.5). High values are preferred as the signal carries higher energy [5].

$$p(\theta, \phi) = \max_t |h^+(t, \theta, \phi)| \quad (2.23)$$

### 2.11.2 Width of the Envelope

The width of the envelope describes the broadening of the radiated impulse and is defined as the width of the magnitude of the analytic envelope at half maximum (FWHM). A small envelope width is desirable (Figure 2.5) [5].

$$\tau_{FWHM} = t_1 \Big|_{|h^+(t_1)|=p/2} - t_2 \Big|_{t_2 < t_1, |h^+(t_2)|=p/2} \quad (2.24)$$

### 2.11.3 Ringing

The ringing of an antenna is the duration of the oscillations after the main peak, which is defined as the time until the envelope has fallen from the peak value  $p(\theta, \phi)$  below a lower bound  $\alpha p(\theta, \phi)$  (Figure 2.5). Desirable is a small ringing [5].

$$\tau_{r=\alpha} = t_1 \Big|_{|h^+(t_1)|=\alpha p} - t_2 \Big|_{t_1 < t_2, |h^+(t_2)|=p} \quad (2.25)$$

### 2.11.4 Group Delay

The group delay  $\tau_g$  of an antenna describes the frequency dependent time delay (Figure 2.6). The parameter of interest is the relative group delay  $\tau_{g,rel}$ , which is the deviation of the group delay from the mean group delay  $\overline{\tau_g}$ . The latter characterizes a trend variation of the group delay over the frequency [5].

$$\tau_g(\omega) = -\frac{d\phi(\omega)}{d\omega} \quad (2.26)$$

$$\overline{\tau_g} = \frac{1}{\omega_2 - \omega_1} \int_{\omega_1}^{\omega_2} \tau_g(\omega) d\omega \quad (2.27)$$

$$\tau_{g,rel} = \tau_g(\omega) - \overline{\tau_g} \quad (2.28)$$

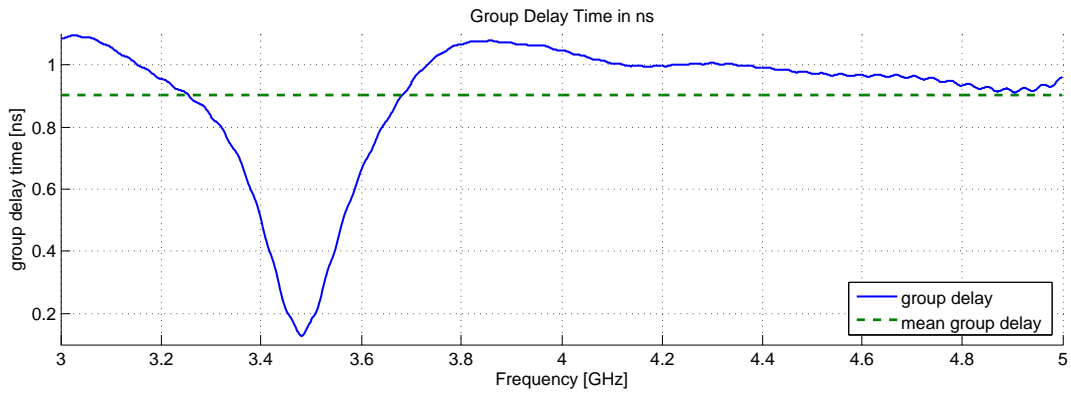


**Figure 2.6:** Impulse response and its envelope of a tapered slot antenna

# 3 Evaluation of Dual- and Circular-Polarized Broadband Antenna Solutions

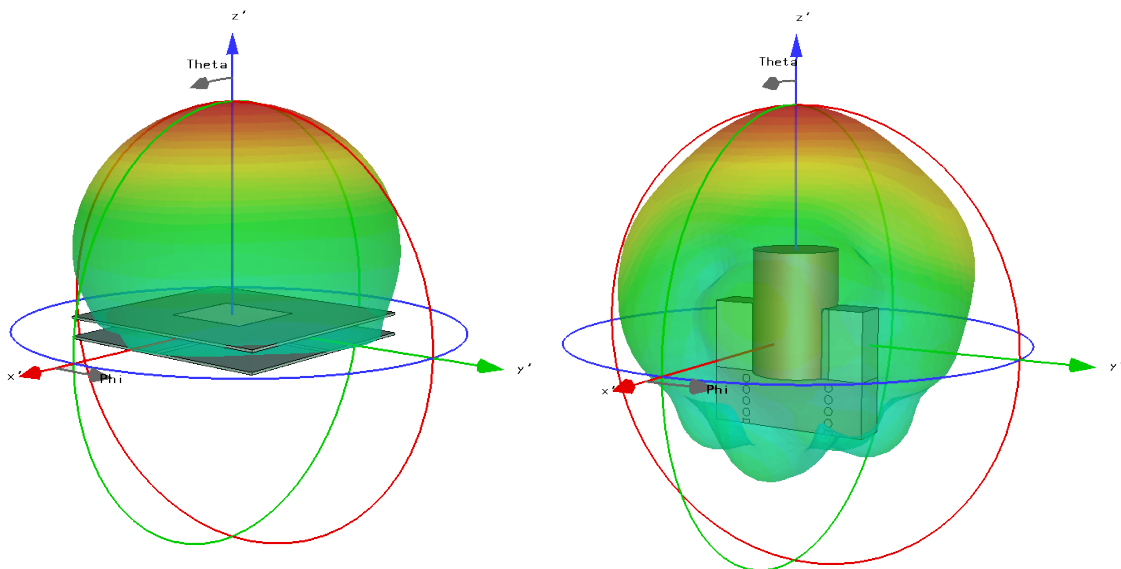
In this chapter, the outcomes of a literature research which has been made according to the requirements in Section 1.2 are documented and discussed.

In the precedent literature research, several designs of circularly-polarized broad-band and ultra-wide band antennas have been gathered using common resources such as the IEEE archives.

To provide a common base for the evaluation of the proposed antennas, the presented designs have been modeled and simulated in CST Microwave Studio (further referred as *CST*, [6]). *CST* provides a variety of three dimensional electromagnetic field solvers in time and frequency domain and integrates a CAD module as well as a toolbox for processing the simulation output.

## 3.1 Coordinate System

All simulated models have been aligned in a way that their main beam points in the direction of the z-axis of the Cartesian coordinate system. This means that broad-side antennas such as the patch antenna (Section 3.5) are placed in the x-y plane and end-fire antennas such as the antipodal tapered slot antenna (Section 3.6) are aligned on the z-axis (Figure 3.1).



(a) broad-side antenna (b) end-fire antenna  
**Figure 3.1:** Alignment of simulated models and their far-field (in CST)

## 3.2 Coplanar Waveguide-Fed Square Slot Antenna

This antenna design (further referred as *slot antenna*) was proposed in [7]. In this paper, the antenna has been dimensioned for a center frequency  $f_c$  between 1965 MHz and 2000 MHz and a 3 dB axial ratio bandwidth in the broadside direction between 18 % and 19 %.

Since not all necessary diagrams have been presented, the antenna was simulated in CST Microwave Studio in order to give a more detailed overview of its performance.

### 3.2.1 Geometry

The proposed geometry is based on a square slot with the length  $L = 40$  mm. The slot is fed by a microstrip which is connected to a  $50\ \Omega$  CPW. To force an orthogonal distribution of the E-Field within the slot (and therefore a circular polarization) and to increase the bandwidth of the antenna, a T-shaped metallic strip is protruded from the left edge of the slot.

The dimensions of this antenna are  $70 \times 70\ \text{mm}^2$

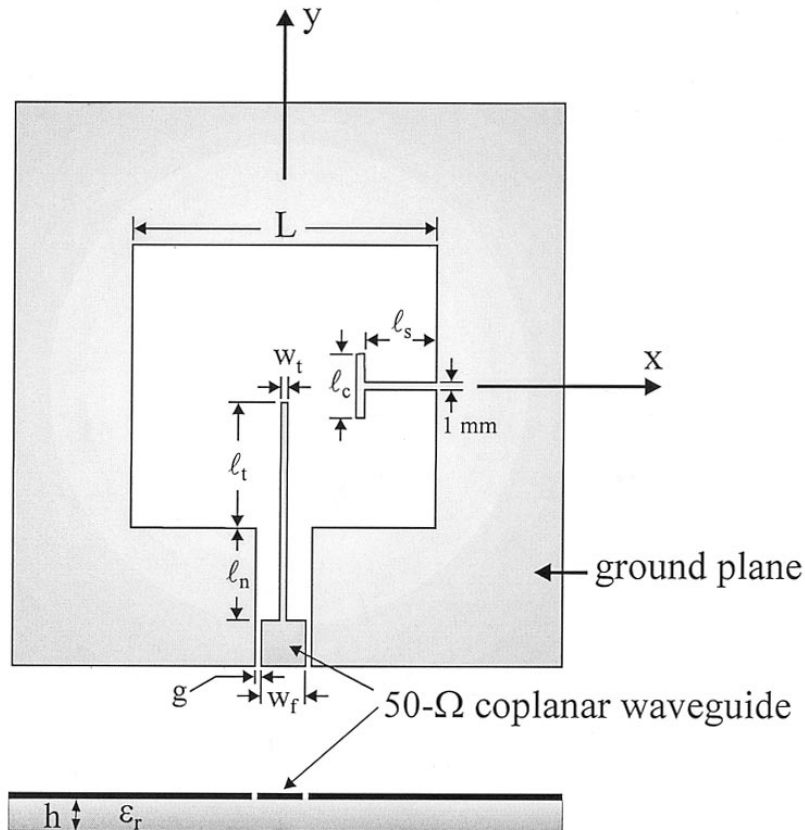
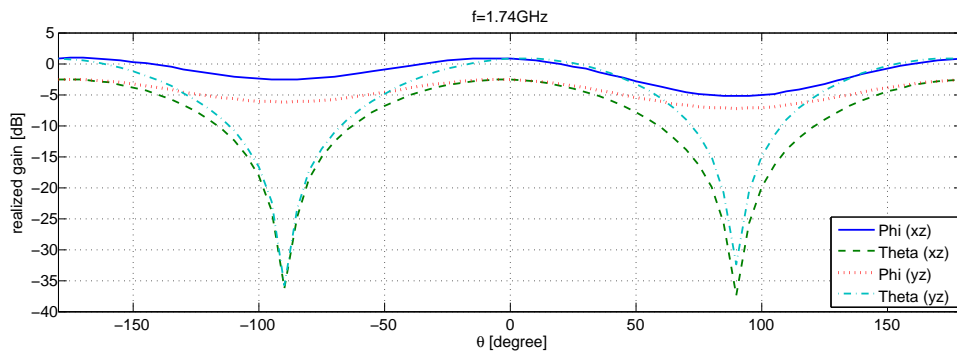


**Figure 3.2:** Geometry of the slot antenna as proposed in [7]

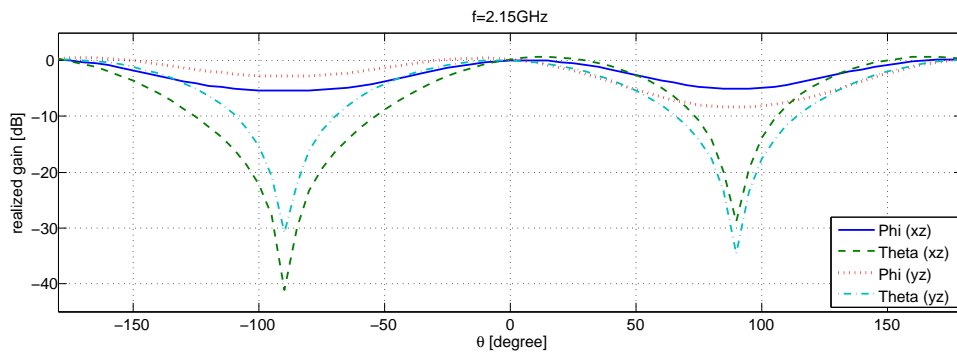
### 3.2.2 Antenna Characteristics

All graphs have been created based on a simulation of the second antenna model presented in [7]. The metallic parts have been assumed to be perfect electrical conductors and the dielectric substrate has been assumed to be loss free.

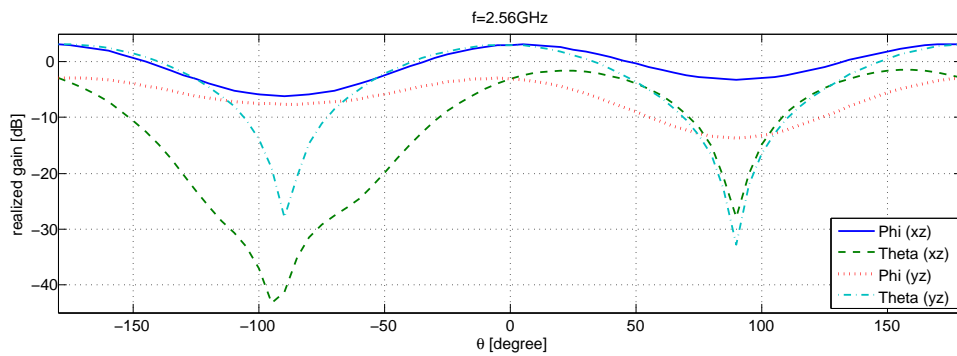
As mentioned in Section 3.1, the antenna has been placed in the  $xy$ -plane. Therefore, the  $xz$ -plane and the  $yz$ -plane represent a sweep of  $\theta$  for  $\phi = 0^\circ$  and  $\phi = 90^\circ$ , respectively. Phi and Theta are the two orthogonal components of the electric field in the given point.



(a) 1.74 GHz



(b) 2.15 GHz



(c) 2.56 GHz

**Figure 3.3:** Realized gain of the slot antenna.

At the center frequency ( $f_c = 2.15$  GHz, middle), the main beam (at  $\theta = 5^\circ$ ,  $86.7^\circ$  wide) shows a good axial ratio (Figure 3.17). For both frequency limits ( $f_1 = 1.74$  GHz, top and  $f_2 = 2.56$  GHz, bottom), the secondary component of the electric field is 1–2 dB smaller than the main component. The asymmetric radiation pattern is caused by the T-shaped ground strip (Figure 3.3).

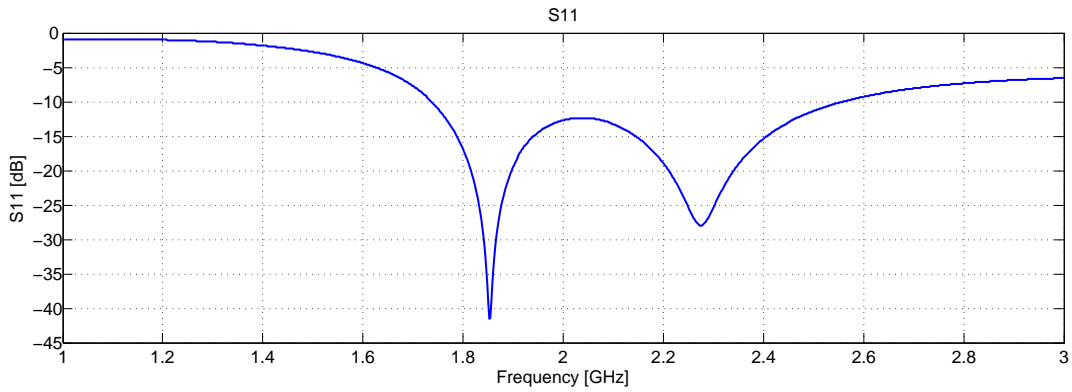


**Figure 3.4:**  $S_{11}$  of the slot antenna over the frequency

As shown in Figure 3.16, there are two resonant frequencies from the two resonating modes which are necessary to obtain the circular polarization ( $f_{R1} = 1.85$  GHz and  $f_{R2} = 2.225$  GHz). The limit frequencies at  $S_{11} = -10$  dB are  $f_1 = 1.74$  GHz and  $f_2 = 2.56$  GHz. The center frequency is  $f_c = 2.15$  GHz.

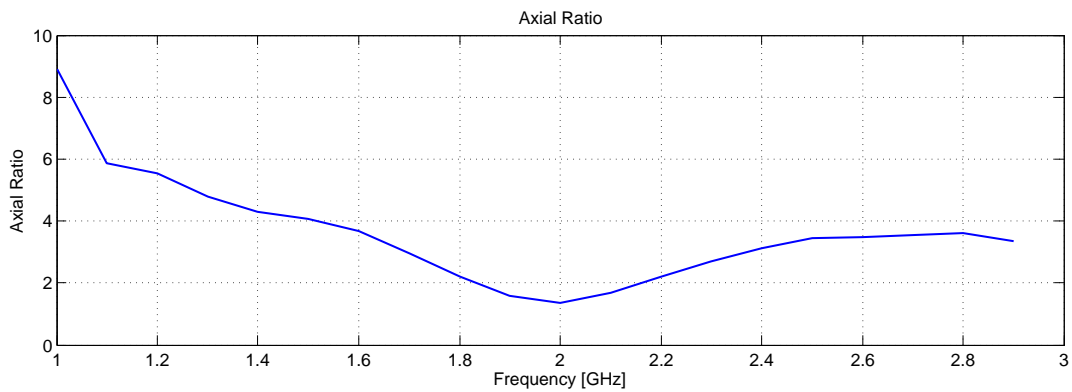


**Figure 3.5:** Axial ratio of the slot antenna over the frequency

### 3.3 L-shaped Probe and L-shaped Wide-Slot Antenna

This antenna design (further referred as *probe antenna*) was proposed in [8]. During the verification of the results which have been presented in the paper, a modification of the impedance matching circuit has been made.

#### 3.3.1 Geometry

In order to excite the two needed components of the electric field ( $E_\theta$  and  $E_\phi$ ), an L-shaped probe is used. The wide slot on the backside of the antenna is used to increase the bandwidth. To improve

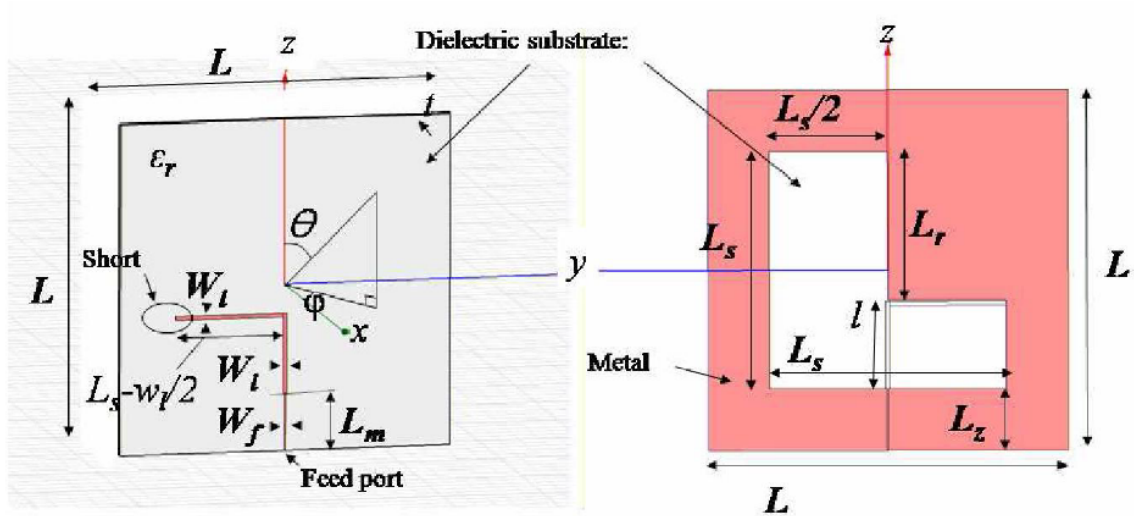
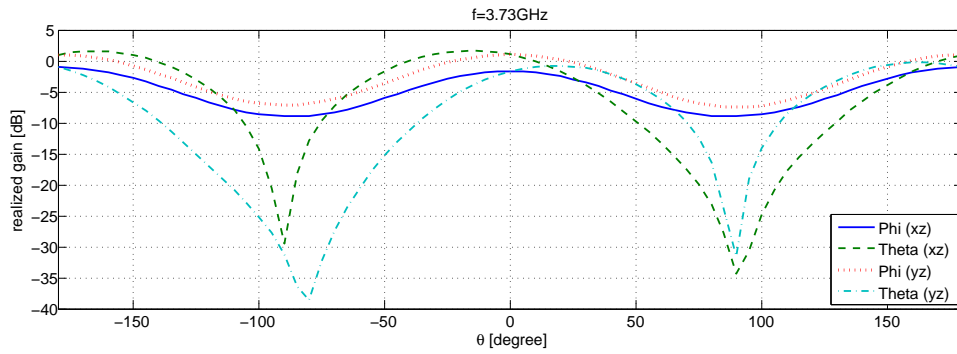


Figure 3.6: Geometry of the probe antenna as proposed in [8]

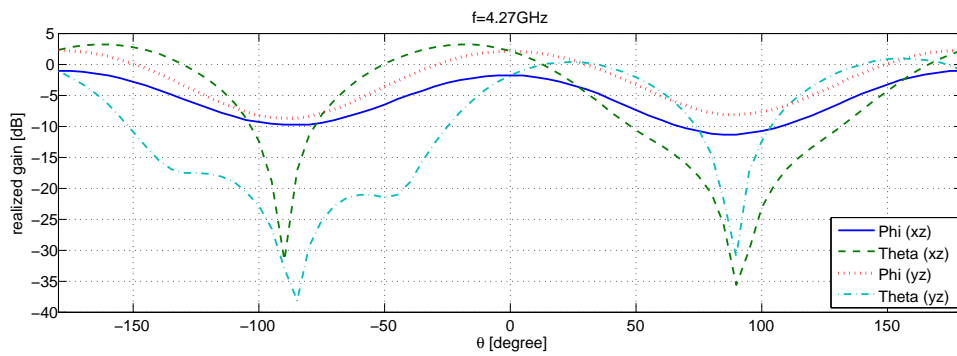
the axial ratio, an L-shaped slot was chosen, to cover the area of  $y < 0$  and  $z < 0$  where the electric field rotates in the counter direction of the circular polarization. The dimensions of this antenna are  $50 \times 50 \text{ mm}^2$

### 3.3.2 Antenna Characteristics

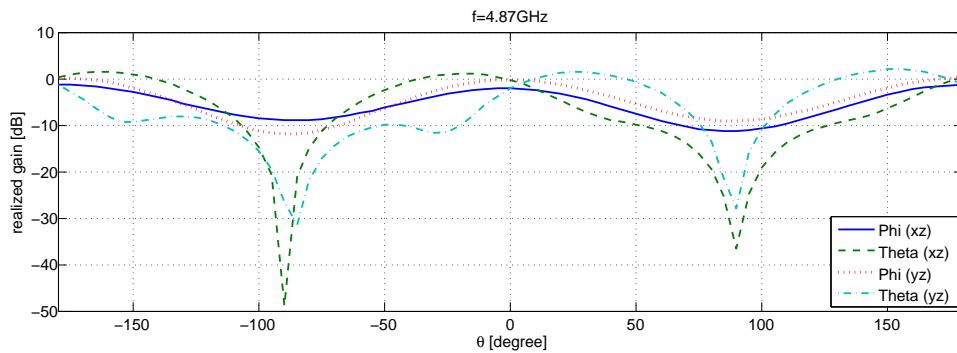
All graphs have been created based on a model of the second antenna model as defined in [8]. The matching structure has been modified in order to match the antenna input impedance to  $50\ \Omega$ .



(a) 3.73 GHz



(b) 4.27 GHz



(c) 4.87 GHz

**Figure 3.7:** Realized gain of the probe antenna.

The pattern shows a non-optimal axial ratio (Figure 3.9) in the main beam ( $\theta = -10^\circ$ ,  $71.2^\circ$  wide). Due to the asymmetric form of the L-shaped slot, the radiation pattern shows a variation of its shape over the frequency range. (Figure 3.7)

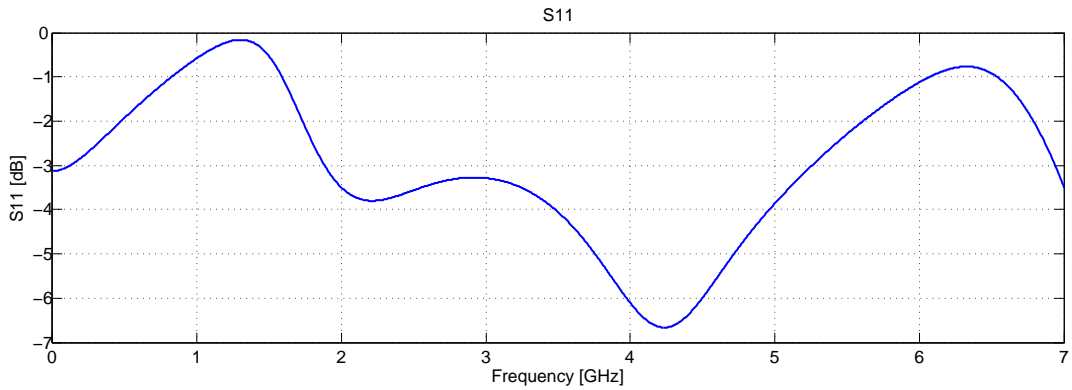


**Figure 3.8:**  $S_{11}$  of the probe antenna over the frequency.

The resonant frequency  $f_R = 4.2$  GHz. The difference of the -10dB-bandwidth between the results in [8] and the presented simulation comes mainly from a mismatching of the feeding circuit (Figure 3.8).

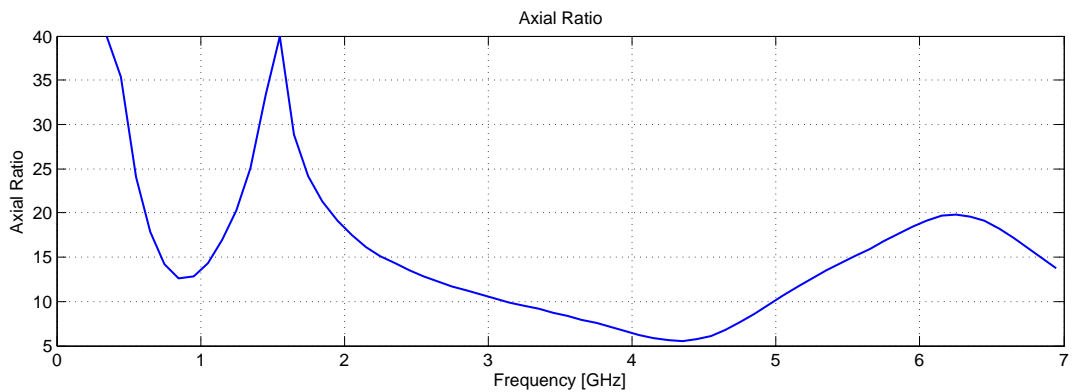


**Figure 3.9:** Axial ratio of the probe antenna over the frequency

### 3.4 Slot/Strip Loop Antenna

This antenna design (further referred as *loop antenna*) was proposed in [9]. The structure is formed by a planar geometry with a metallic back cavity to improve the bandwidth.

#### 3.4.1 Geometry

The antenna design is a combination of a slot and a strip loop. Both are radiating a circularly polarized wave on two different center frequencies. The feeding structure is a  $50\ \Omega$  microstrip line with a coupling stub and an open stub to match the impedance. The dimensions of this antenna are  $62 \times 36\ \text{mm}^2$

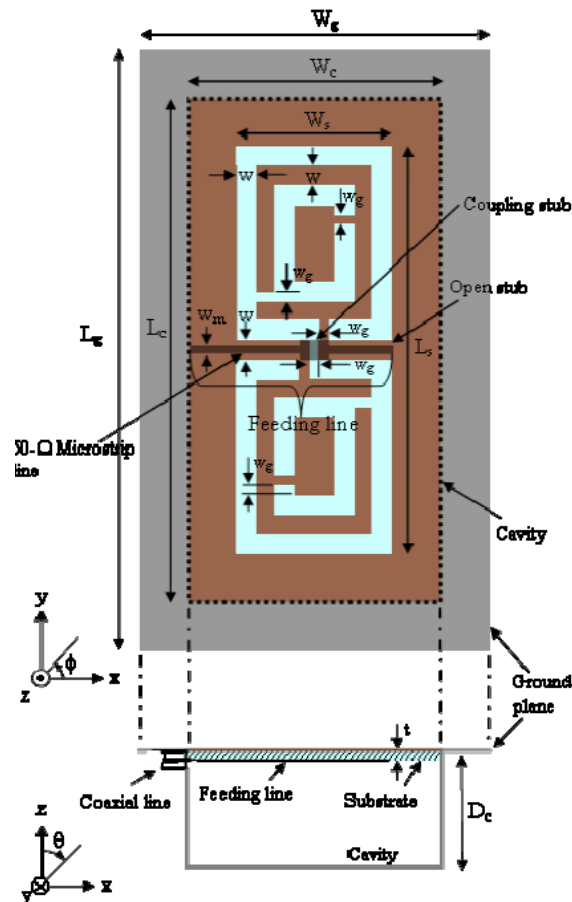
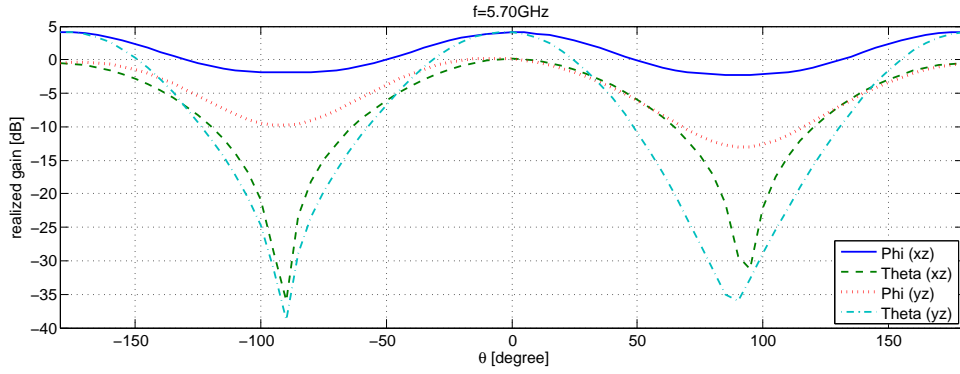


Figure 3.10: Geometry of the slot/strip loop antenna as proposed in [9]

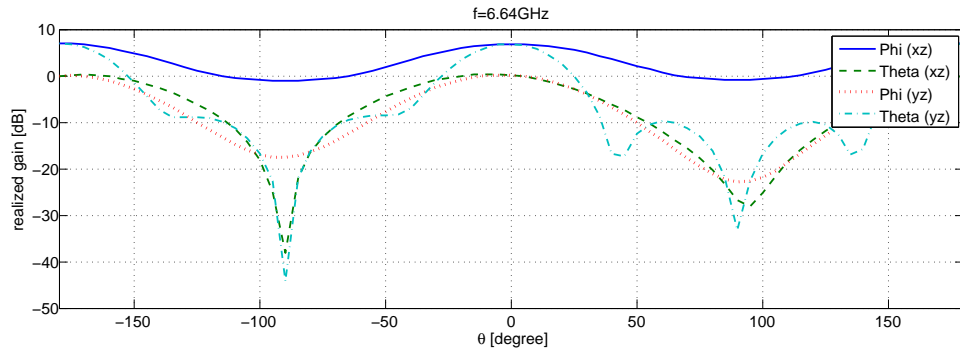
#### 3.4.2 Antenna Characteristics

All graphs have been created based on a of the slot/strip loop antenna, proposed in [9]. The metallic parts have been assumed to be perfect electrical conductors and the dielectric substrate has been assumed to be loss free. To comply with the requirements of the thesis in terms of planarity and thin structure, the cavity has been neglected during the simulations.

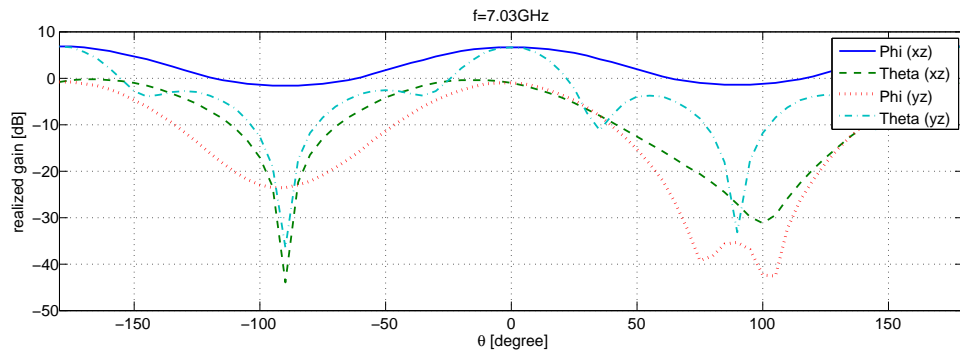
The radiation pattern (Figure 3.11) shows a relatively narrow main beam width ( $37.4^\circ$  at  $\theta = -7.7^\circ$ ) and a relatively high gain (6dB in the main beam direction).



(a) 5.70 GHz



(b) 6.64 GHz



(c) 7.03 GHz

**Figure 3.11:** Realized gain of the loop antenna; top: 5.7 GHz, middle: 6.64 GHz, bottom: 7.03 GHz

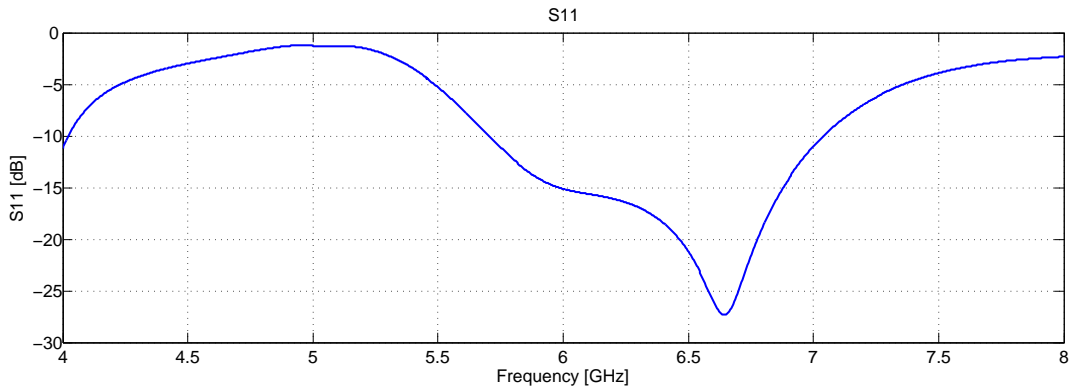


**Figure 3.12:**  $S_{11}$  of the loop antenna over the frequency

The two resonant frequencies ( $f_{R1} = 6\text{GHz}$  and  $f_{R2} = 6.64\text{GHz}$ ) are caused by the two loops of the antenna design. The two -10dB-limit frequencies are at  $f_1 = 5.7\text{GHz}$  and  $f_2 = 7.03\text{GHz}$  (Figure 3.12).

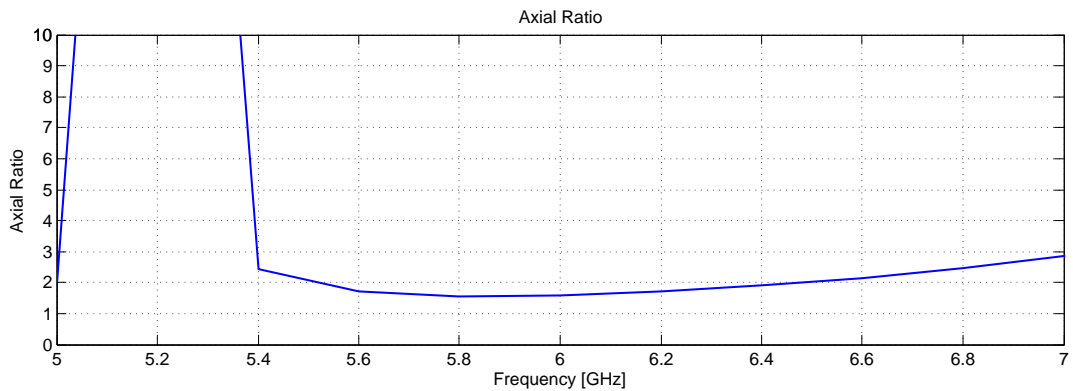


**Figure 3.13:** Axial ratio of the loop antenna over the frequency.

The axial ratio (Figure 3.13) shows a quite stable behavior over the usable frequency range (5.5–6.5GHz).

### 3.5 Circularly Fed Patch Antenna

The original antenna (further referred as *patch antenna*) was proposed in [10]. To ease up the simulations, the bottom foam layer was neglected. The feeding via coaxial probes were also replaced by microstrip feeds. This leads to a reduction of the bandwidth, as well as a reduction of the maximum gain, because of the narrowband feeding method.

#### 3.5.1 Geometry

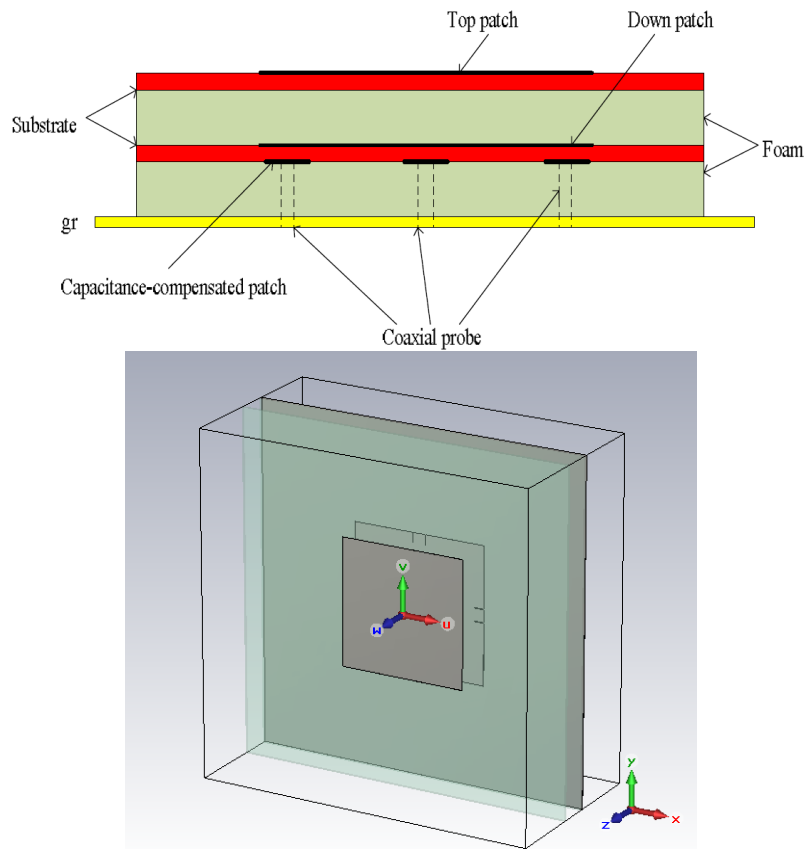
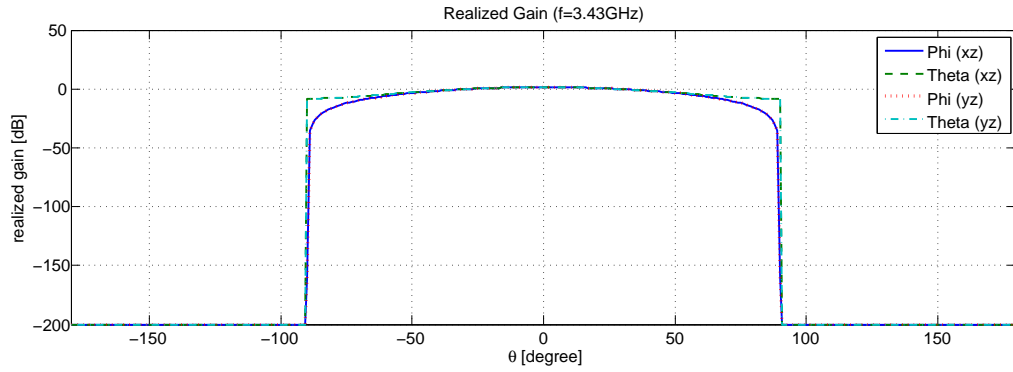


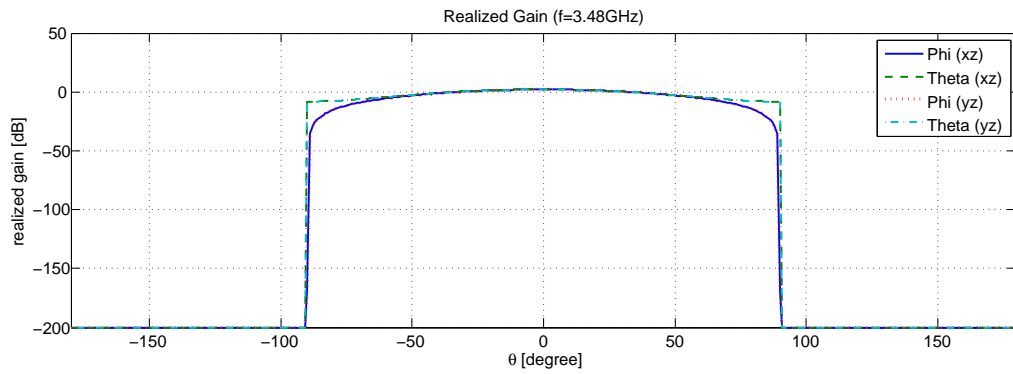
**Figure 3.14:** Geometry of the patch antenna as proposed in [10]

The antenna consists of two patches separated by a foam layer. The bottom patch is fed by 4 micro-strip lines which have a geometrical and an electrical phase-shift of 90 degrees. This feeding technique ensures a stable phase center and a low axial ratio. Due to the change of the feeding technique, the bottom foam layer has been neglected. The dimensions of this antenna are  $50 \times 50 \text{ mm}^2$

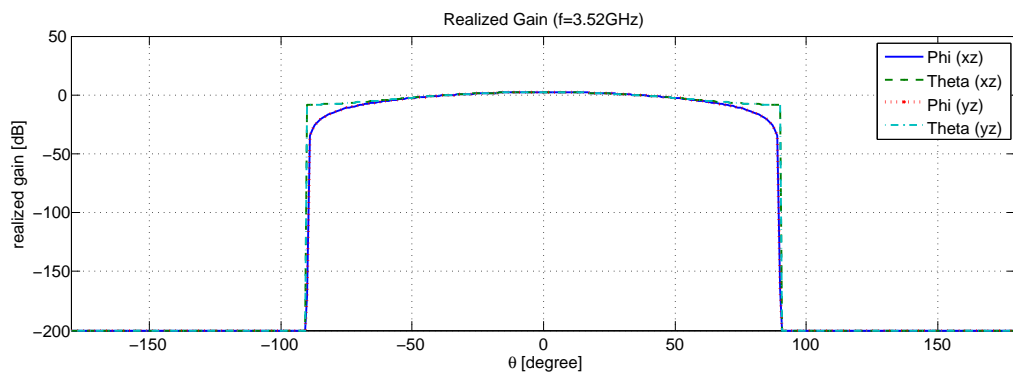
### 3.5.2 Antenna Characteristics



(a) 3.43 GHz



(b) 3.48 GHz



(c) 3.52 GHz

**Figure 3.15:** Realized gain of the patch antenna.

The radiation pattern shows a main beam at  $\theta = 0^\circ$  with a width of  $79.5^\circ$  (Figure 3.15). Due to the feeding technique, the bandwidth of the simulated model is very small. Still, the two resonant frequencies ( $f_{R1} = 3.5$  GHz and  $f_{R2} = 3.95$  GHz) are visible. These resonant frequencies are related to the different sizes of the two patches (Figure 3.16).

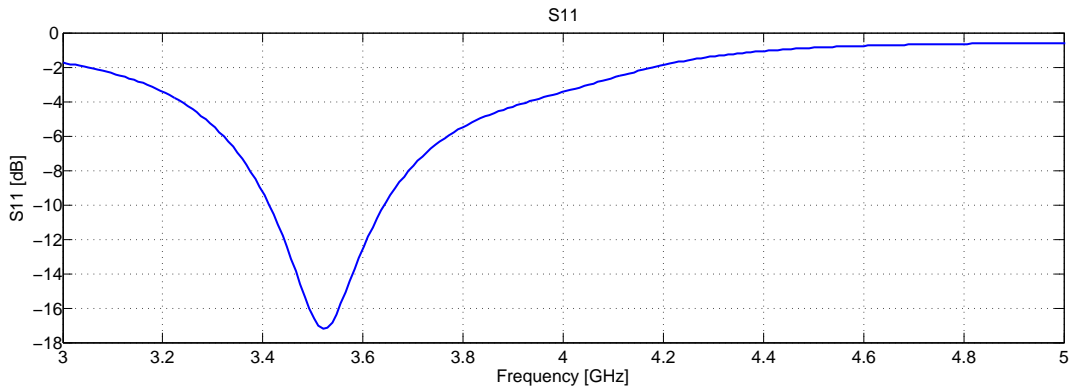


**Figure 3.16:**  $S_{11}$  of the patch antenna over the frequency

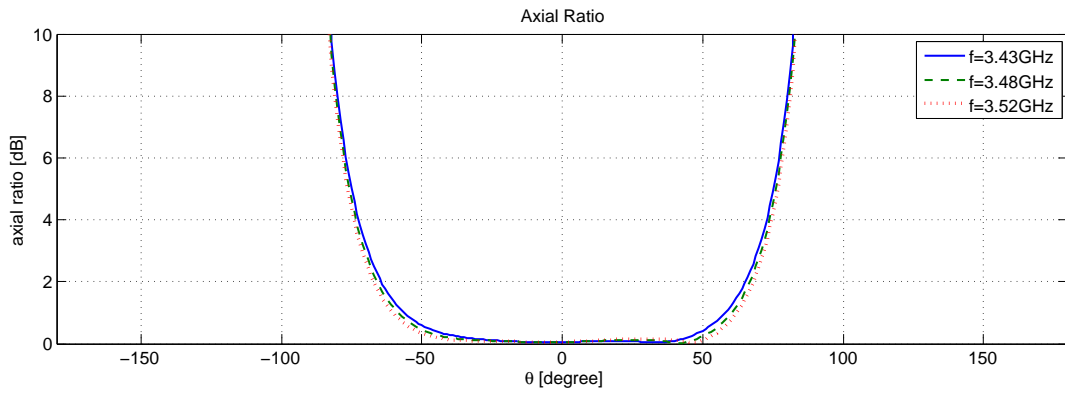


**Figure 3.17:** Axial ratio of the patch antenna at different frequencies

The patch antenna shows a very stable behavior of its axial ratio over the frequency range (Figure 3.17).

### 3.6 Antipodal Tapered Slot Antenna

In contrast to the previous presented antennas, this antenna (further referred as *tapered slot antenna*) which has been proposed in [11], is an end-fire radiator. Also, this antenna design cannot be mounted directly on a metal surface to avoid shorting the electric field of the radiator.

#### 3.6.1 Geometry

This antenna design uses a linearly tapered slot antenna (TSA) which has a linear-polarized wide-band end-fire radiation. Instead of the common CPW feed, a substrate integrated waveguide (SIW) is used to excite the TSA with a  $TE_{11}$ -like mode.

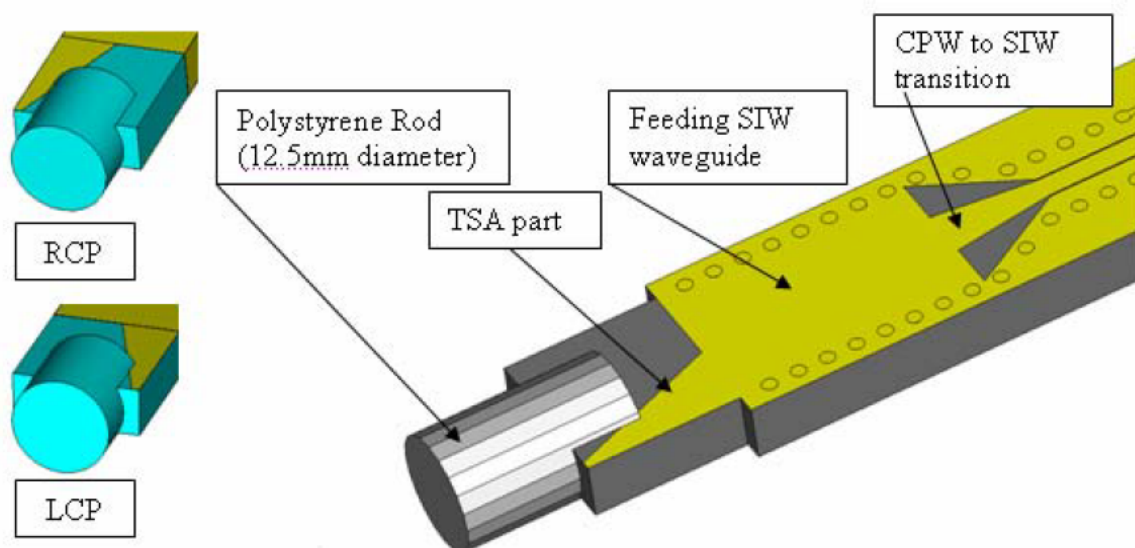


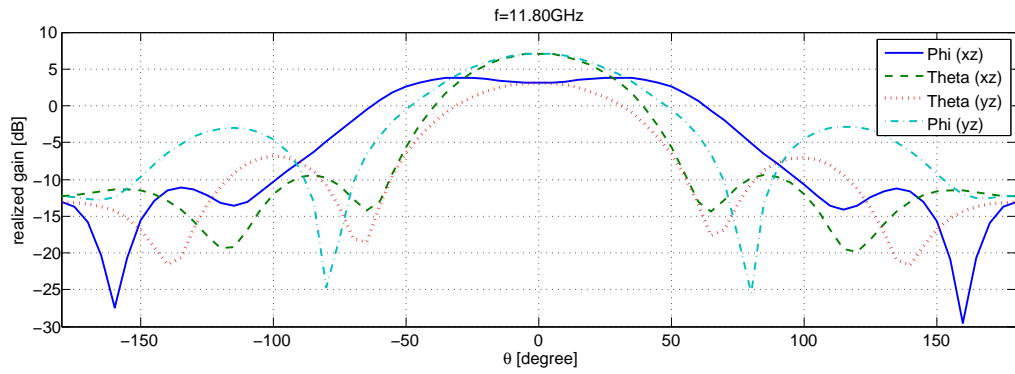
**Figure 3.18:** Geometry of the tapered slot antenna as proposed in [11]

Using a relatively thick substrate, a circular polarization can be achieved. The protruded polystyrene rod is used to increase the axial ratio bandwidth of the antenna itself.

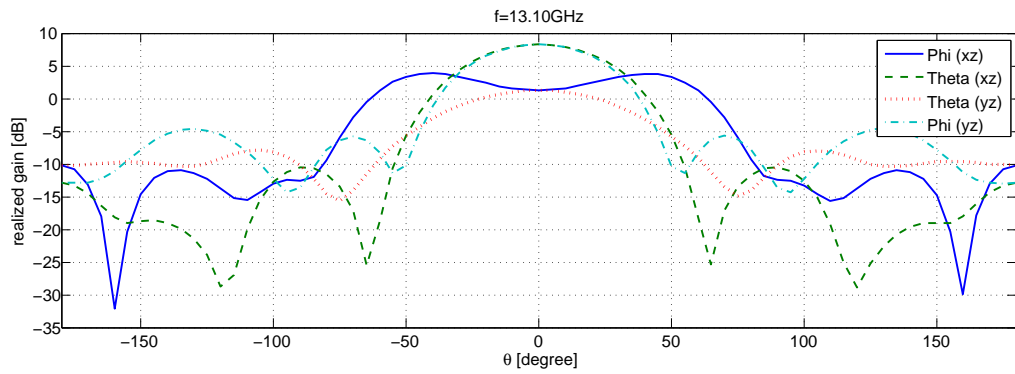
#### 3.6.2 Antenna Characteristics

To create the graphs for the antipodal tapered slot antenna, the design presented in [11] has been reproduced. To simplify the model, the feeding structure has been replaced by a waveguide-port which excites the substrate integrated waveguide.

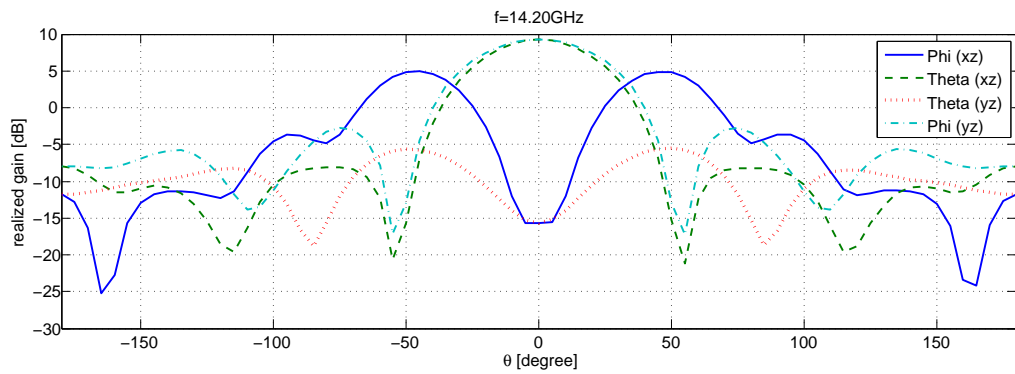
The antenna shows good performances in the main beam direction ( $\theta = 0$ ,  $73.8^\circ$  wide at 11.80 GHz) and a good axial ratio in the lower frequency range. Due to the lack of information regarding some geometrical parameters, a slightly different input reflection coefficient has been obtained with respect to the results in [11]



(a) 11.80 GHz



(b) 13.10 GHz



(c) 14.20 GHz

**Figure 3.19:** Realized gain of the antipodal tapered slot antenna.

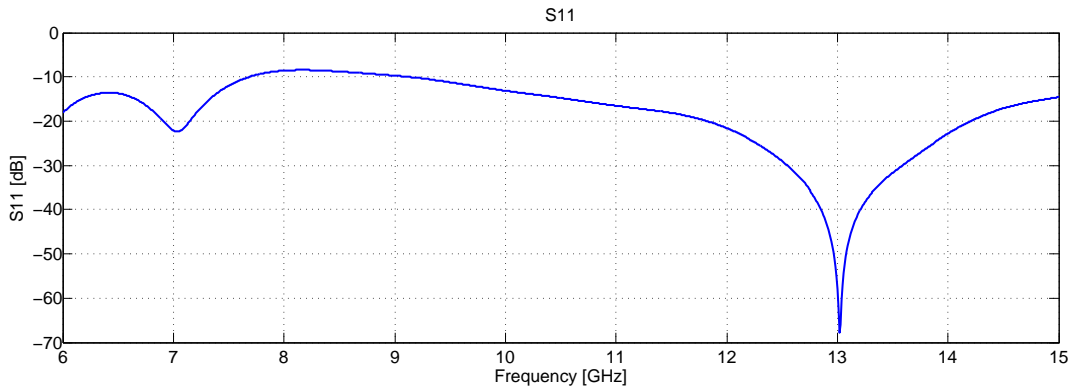


**Figure 3.20:**  $S_{11}$  of the antipodal tapered slot antenna over the frequency

The reflection coefficient of the tapered slot antenna shows the typical behavior of a tapered slot antenna (Figure 3.20). The shift of the center frequency with the optimal matching can be explained by the mismatch between the simulation model and the presented design.

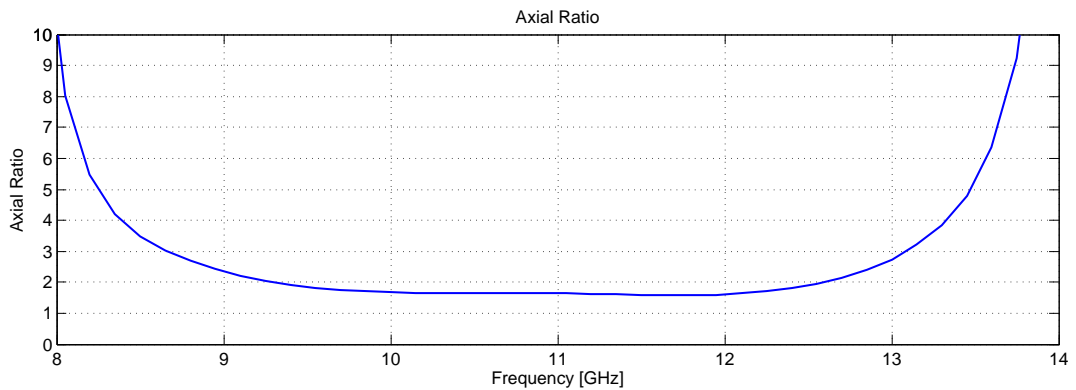


**Figure 3.21:** Axial ratio of the antipodal tapered slot antenna

As already mentioned before, the antenna shows a good axial ratio (Figure 3.21) for a relatively wide frequency range (9 – 13GHz). Differently to the presented design, there is a shift between the center frequency of the matching and the center frequency of the axial ratio.

### 3.7 Comparison and Summary of the analyzed Antennas

Table 3.1 compares the proposed antenna designs which have been described in the previous sections. Besides geometrical parameters such as the overall dimension and the number of feeds, the input impedance bandwidth and far-field pattern parameters have been used as criteria for this comparison.

Characteristic	Slot	Probe	Loop	Patch	Tapered Slot
Number of ports	1	1	1	4	1
Dimensions [mm <sup>3</sup> ]	70 × 70 × 1.7	41 × 41 × 0.9	62 × 36 × 0.3	70 × 70 × 12.7	85 × 47 × 12.5
Center frequency [GHz]	1.96	5.5	6.35	3.35	10
Bandwidth [MHz]	865	2500	1270	1700	2900
Relative bandwidth [%]	44.1	45.5	20.0	50.7	29.0
Main beam direction	broad-side	broad-side	broad-side	broad-side	end-fire
Main beam direction tilt [ $\theta$ /Degree]	5	10	0	0	0
Main beam width [Degree]	86.7	71.2	37.4	79.5	60
Main lobe magnitude [dB]	3.3	4.2	7.7	5.0	9.1

**Table 3.1:** Comparison of circular and dual polarized broadband antennas

According to Table 3.1, two antenna designs, the patch antenna and the tapered slot antenna, have been selected to be implemented.

**Patch antenna** This antenna is the only proposed design which has more than one excitation port.

Due to this feeding technique, the antenna provides a very stable behavior of the axial ratio in the frequency domain, as well as in the radiation characteristics.

**Tapered Slot antenna** This design is the only end-fire antenna which has been evaluated. Besides that, the design provides a wide bandwidth for the reflection coefficient as well as for the axial ratio.

Table 3.2 lists advantages and disadvantages of the recommended antennas, including the perspectives manufacturing and operation, which have not been discussed so far, but have influenced the final decision.

Characteristic	Patch	Tapered Slot
Grounded backplane	yes	no
Beam direction	broadside	end-fire
Feeding	complex	simple
Feeding Ports	4	1
Axial Ratio	very good	good
Manufacturing	easy	complex

**Table 3.2:** Advantages and disadvantages of the recommended antenna designs

## 4 Implementation of the Dual-Polarized Patch Antenna

The requirement of a low profile antenna suggests the usage of a microstrip structure. These antennas do not only provide a compact design, but they are also easy and cost-efficient to manufacture.

However, they usually have a very narrow impedance bandwidth. To overcome this issue, different broadband feeding techniques have been introduced in the past [12, 13, 14, 15].

Differently from the circular-polarized patch antenna presented in Section 3.5, an aperture-coupled dual-fed antenna design has been chosen [16]. This decision was made because this design allows an easier manufacturing process compared to other designs.

### 4.1 Design Elements

The basic design of this antenna has been presented together with the dual-fed square ring slot in [16]. It consists of three main parts: the patch (Figure 4.2a), the slot plane (Figure 4.2b) with the feeding network (Figure 4.2c) and the reflector. These parts are separated by air layers. They ensure a correct distance between feed and reflector and increase the impedance bandwidth of the patch antenna itself.

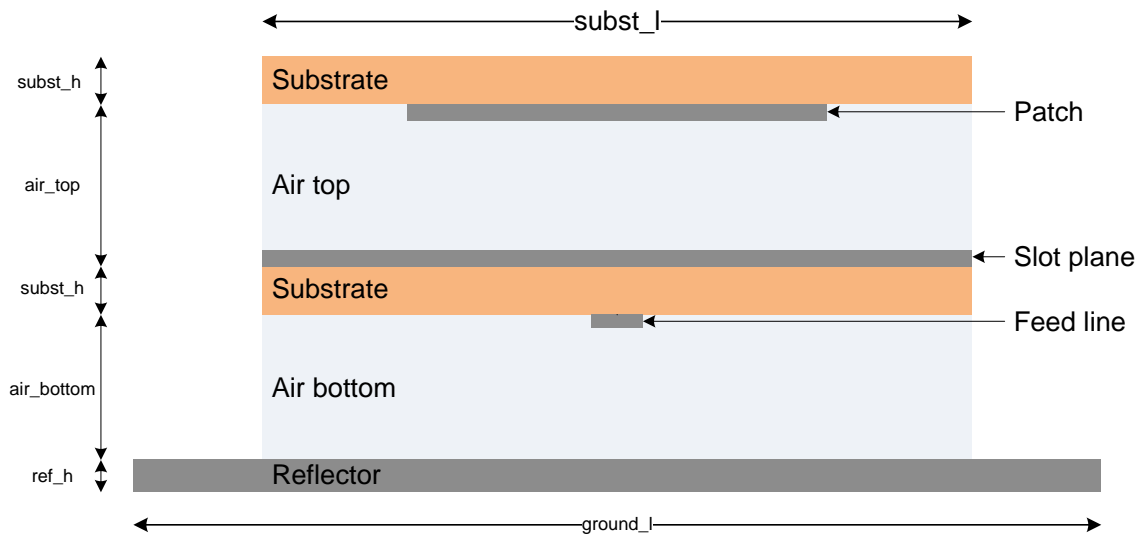
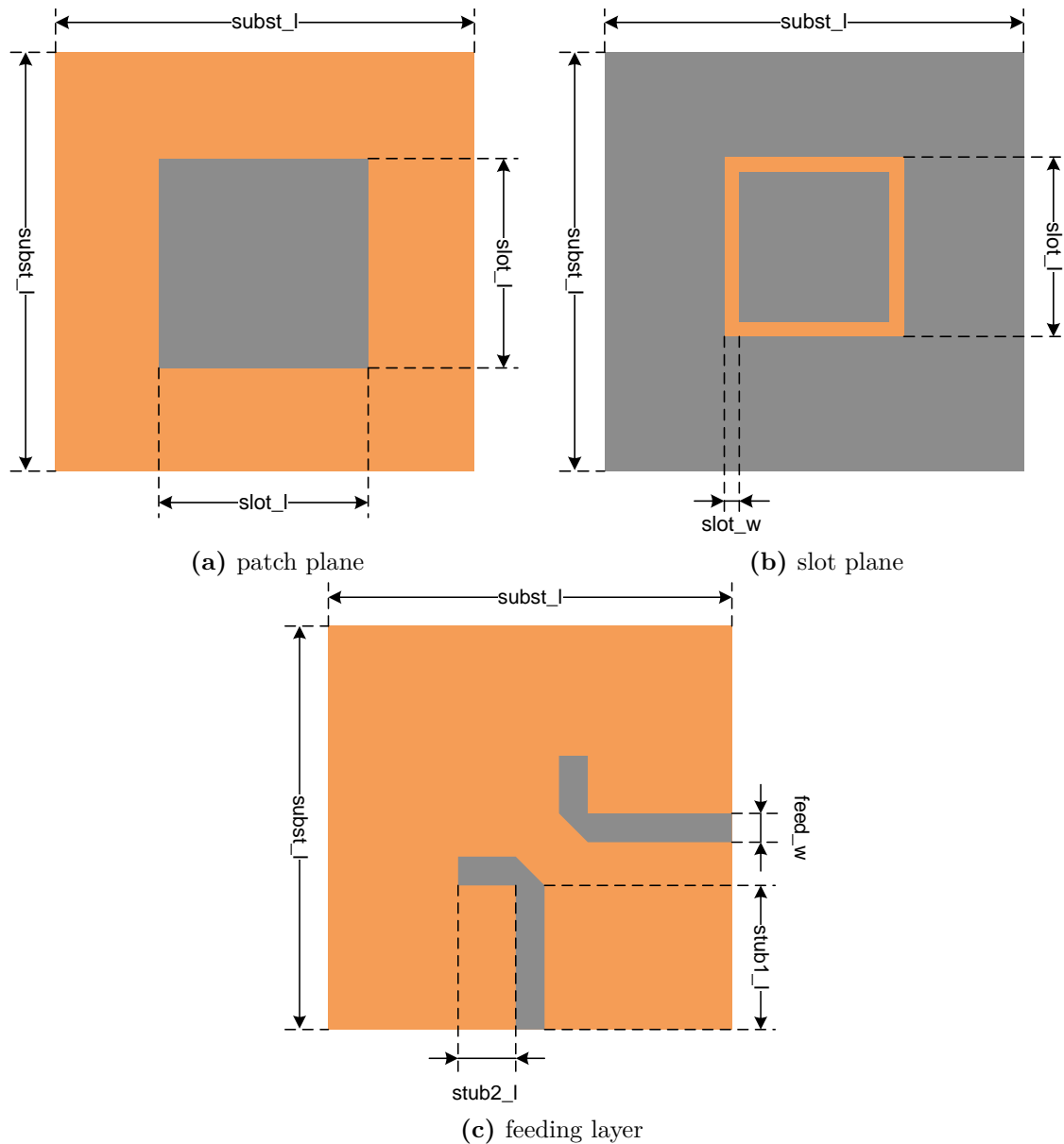


Figure 4.1: Stack up of the dual-polarized patch antenna.

#### 4.1.1 Patch

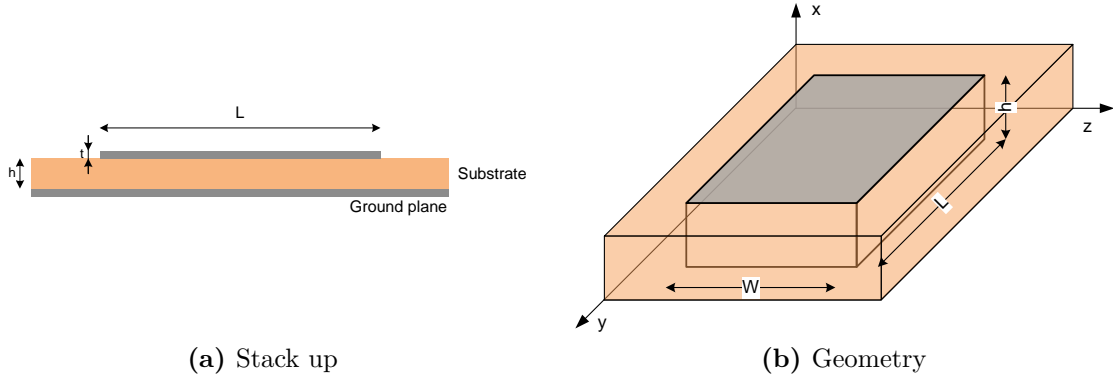
Patch antennas consist of a very thin ( $t \ll \lambda_0$ , where  $\lambda_0$  is the free-space wavelength of the resonant frequency) metallic strip (patch) placed above a ground plane. The strip and the ground plane



**Figure 4.2:** Geometries of the two layers of the dual-polarized patch antenna.

are usually separated by a thin dielectric substrate. The length of a rectangular patch is usually  $\lambda_0/3 \leq L \leq \lambda_0/2$  (Figure 4.3). Due to a properly excited mode beneath the patch, the antenna is radiating towards the broadside direction (the maximum of the radiating pattern is normal to the patch) [2].

Using the cavity model, a patch antenna can be described as a dielectric loaded cavity with electric conductors on top and bottom and perfect magnetic conductors as sidewalls (as open circuit condition) around the patch (Figure 4.4b). Using this boundary conditions, the field configuration within the cavity can be calculated using the vector potential  $A_x$  (Equation 4.1). Depending on the geometrical parameters of the patch antenna, the dominant mode can be either:  $TM_{010}^x$  (Figure 4.5a) if  $L > W > h$



(a) Stack up (b) Geometry  
**Figure 4.3:** Stack-up and Geometry of a simple rectangular patch antenna [2].

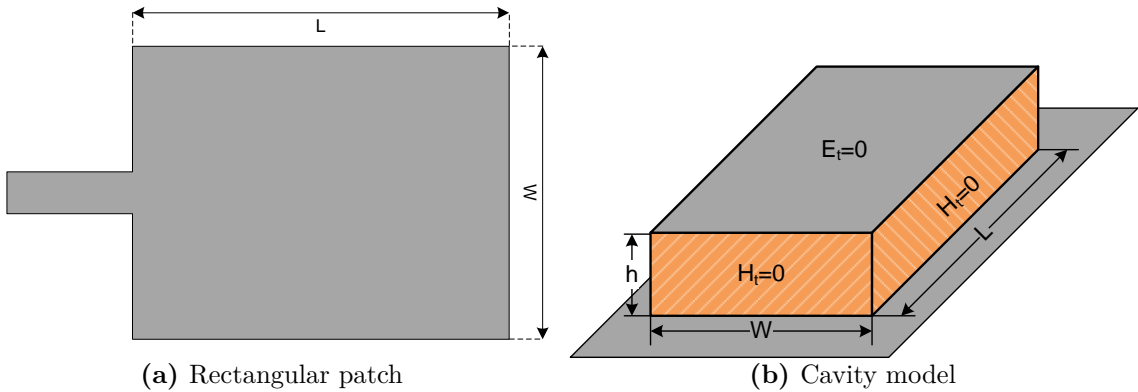
or  $TM_{001}^x$  (Figure 4.5b) if  $W > L > h$  [2].

$$\nabla^2 A_x + k^2 A_x = 0 \quad (4.1)$$

$$f_{res,010} = \frac{1}{2L\sqrt{\mu\epsilon}} = \frac{\nu_0}{2L\sqrt{\epsilon_r}} \quad (4.2)$$

$$f_{res,001} = \frac{1}{2W\sqrt{\mu\epsilon}} = \frac{\nu_0}{2W\sqrt{\epsilon_r}} \quad (4.3)$$

where  $\nu_0$  is the speed of light.



(a) Rectangular patch (b) Cavity model  
**Figure 4.4:** Rectangular patch antenna and its equivalent cavity model [2].

For  $W = L$ , both modes have the same resonant frequency, which allows both modes to be excited at the same time. However, depending on the position of the feed, only one of them will be excited. Assuming that the patch is fed from the  $y$  direction, the  $TM_{010}^x$  mode will be excited.

We assume that

$$L = \frac{\lambda}{2} \quad (4.4)$$

the calculation of the magnetic current densities ( $\mathbf{M}_s$ ) along the sidewalls of the cavity shows that the current densities along the walls in  $z$ -direction have the same magnitude and phase, while the current densities along the walls in  $y$ -direction cancel each other. These current densities can be seen as magnetic dipoles which represent the two radiating slots. The constructive interference of the field radiated by the two slots results in the overall transmitted field in the  $x$ -direction.

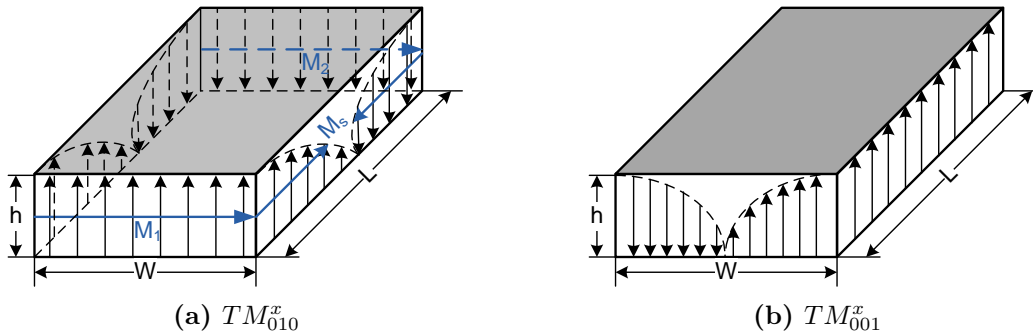


Figure 4.5: Field configurations (modes) for a simple patch [2].

### 4.1.2 Feeding Structure

Together with the microstrip line, the coaxial probe and the proximity coupling, the aperture coupling is one of the most popular feeding techniques. Due to the non-contacting feeding approach, the aperture coupling overcomes the inherent asymmetries of the microstrip line and coaxial probe feeding techniques [2].

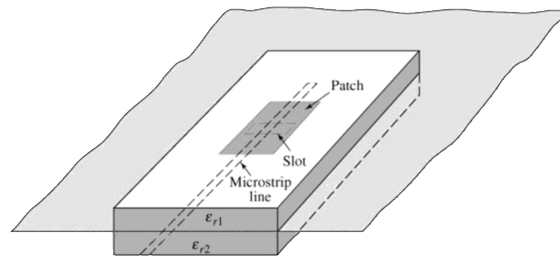


Figure 4.6: Aperture coupled feed [2].

As shown in Figure 4.6, this feeding technique consists of two dielectric substrates which are separated by a ground plane. On the bottom of the lower substrate, a microstrip feed line is coupled to the patch through a slot in the ground plane. Since the feeding structure and the patch are electrically isolated, an independent optimization of the feed mechanism and the radiating element is possible. Additionally, the ground plane eliminates interfering radiations from the feed [17].

The impedance matching of the aperture coupled feed is mainly achieved by adjusting the size (length) of the slot, as well as through the width of the microstrip feed and the length of an open stub which terminates the feeding line after the aperture (see Figure 4.6).

To achieve a circular polarization of the dual-polarized patch antenna, the two rectangular feeds (Figure 4.2c) should be excited with  $90^\circ$  phase-shift and same amplitude.

### 4.1.3 Reflector

Idealizing the reflector to a perfectly conducting sheet of infinite extend with a distance of  $S$  to the antenna, the reflector can be replaced by an image of the antenna with a distance of  $2S$  to the antenna itself (Figure 4.7a). The combination of the antenna and its image leads to an increase of the maximum gain in the main direction (Figure 4.7b) [18].

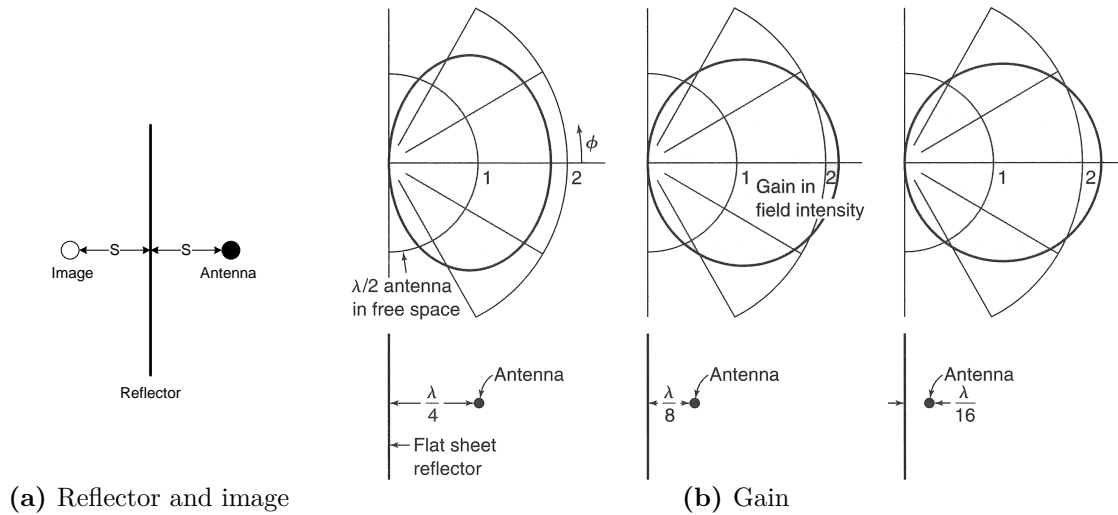


**Figure 4.7:** Antenna with a flat reflector and gain for different distances [18].

For the dual-polarized patch antenna, only the field radiated by the microstrip feed is reflected by the metal sheet, as the field of the patch antenna is already reflected by the grounded slot plane of the feeding structure (Figure 4.1).

## 4.2 Parametric analysis of the design elements

In this Section, the effects of the variation of the design parameters of the dual polarized patch antenna (Figure 4.1 and 4.2), on the input reflection ( $S_{11}$ ) and on the radiation pattern (in terms of realized gain on the  $xz$ -plane) are examined.

### 4.2.1 Patch Parametrization

The variation of the length of the radiating patch (`patch.1`) in figure 4.8 shows a movement of the higher resonating frequency. This frequency corresponds with the resonant frequency of the radiating patch (Equation 4.2).

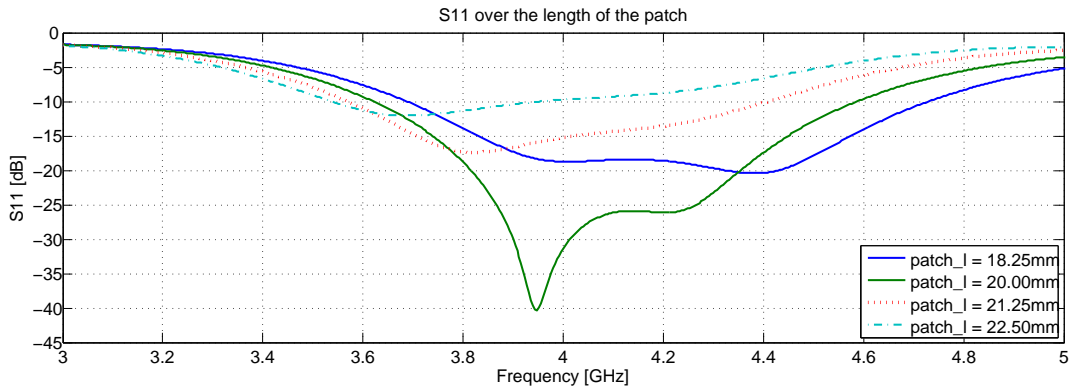


**Figure 4.8:** S11 with respect to the variation of the patch length (`patch_l`).

In Figure 4.9, the variation of the height of the patch antenna (`air_top`) shows a change of the resonant frequency of the patch. For high values of the air thickness (`air_top` > 10mm), the coupling between the feeding structure and the patch tears down and only one resonant frequency of the feeding slot is left. The change of the resonant frequency can be explained as a change in the fringing effect which causes a variation of the effective dielectric constant  $\epsilon_{eff}$  over the frequency [2].

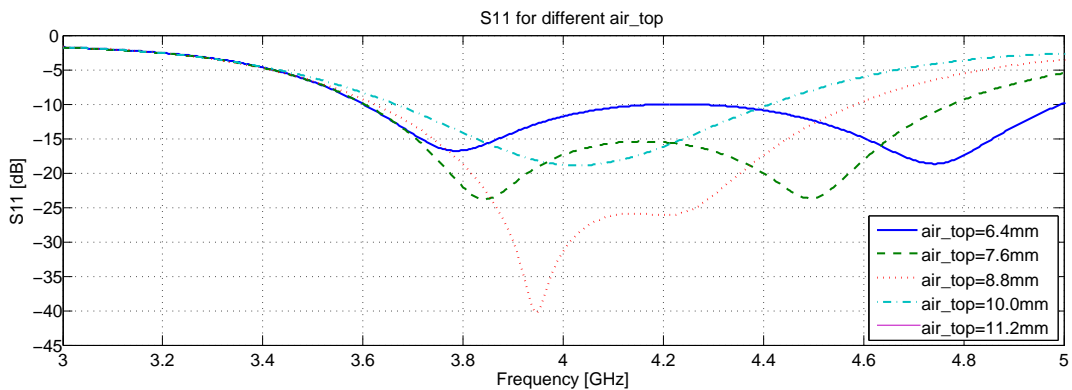


**Figure 4.9:** S11 with respect to the variation of the patch height (`air_top`).

### 4.2.2 Feeding Structure Parametrization

As shown in Figure 4.10, the variation of the length of the squared slot causes a shift of its resonant frequency. The closer the slot resonance moves to the resonating frequency of the patch, the more the absolute matching improves and the bandwidth decreases.

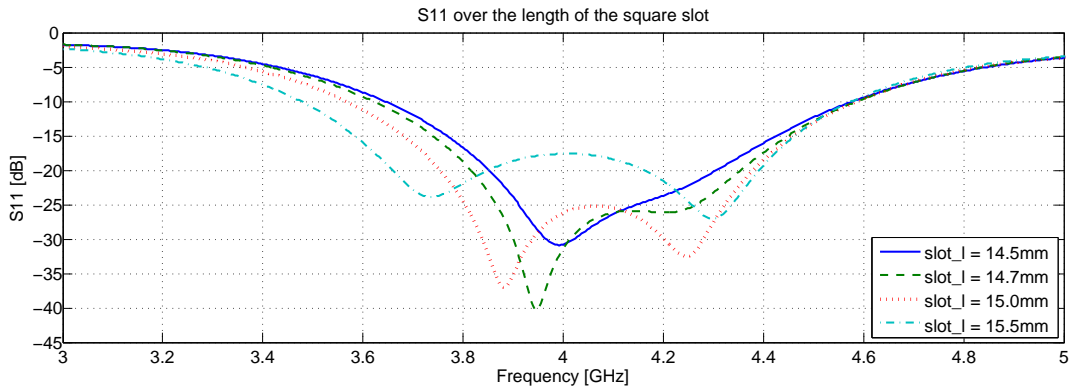


**Figure 4.10:** S11 with respect to the variation of `slot_l`.

Figure 4.11 shows that the variation of the width of the microstrip-line causes a change of the input impedance and therefore a change of the absolute matching of the antenna.

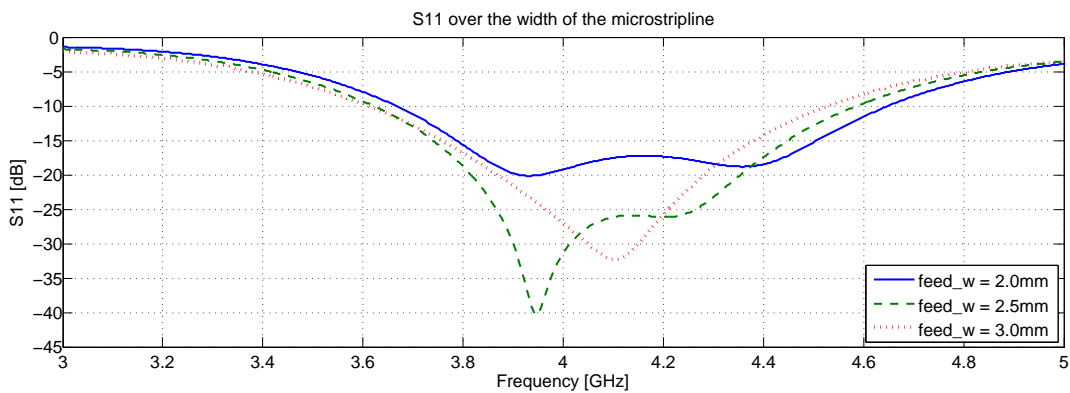


**Figure 4.11:** S11 with respect to the variation of `feed_w`.

Varying the length of the terminating open stub (Figure 4.12) causes a change of the imaginary part of the antenna input impedance. This brings a change of the overall matching towards the reference impedance ( $50 \Omega$ ).

The variation of the size of the grounded slot plane in Figure 4.13 shows less directivity for smaller sizes, while, for higher values, the maximum gain in the main beam direction increases and the back-lobe level decreases.

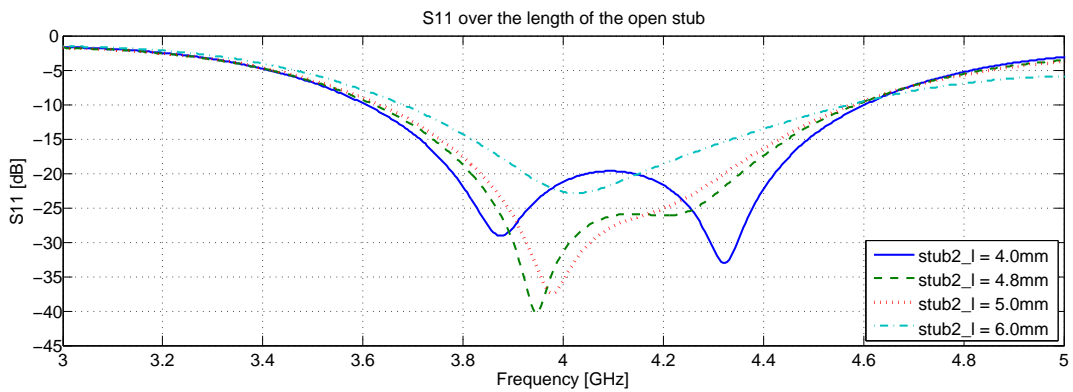
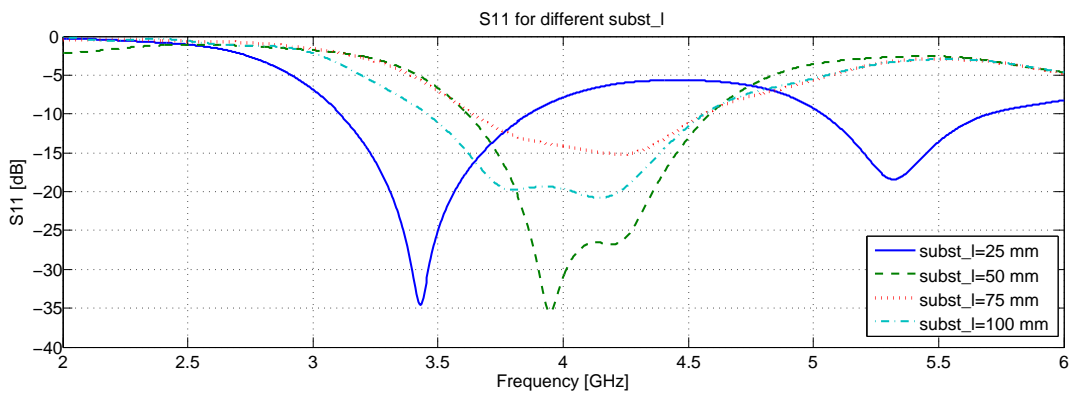
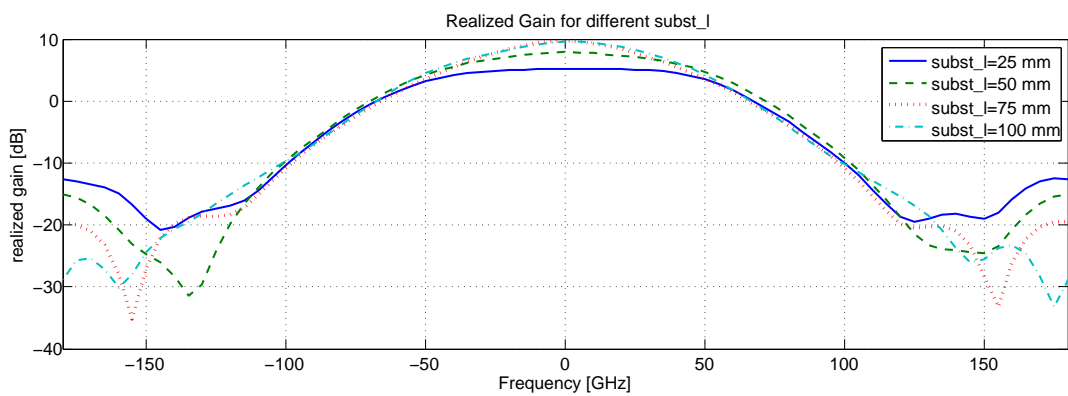


Figure 4.12: S11 with respect to the variation of `stub2.l`.



(a)

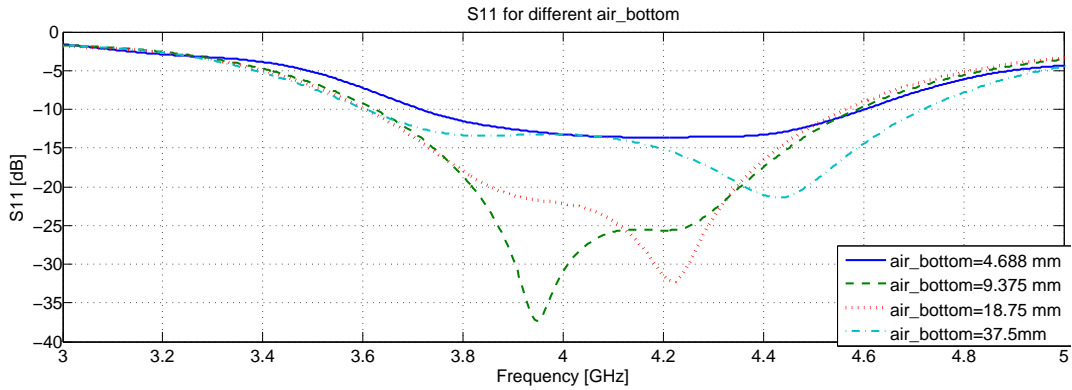


(b)

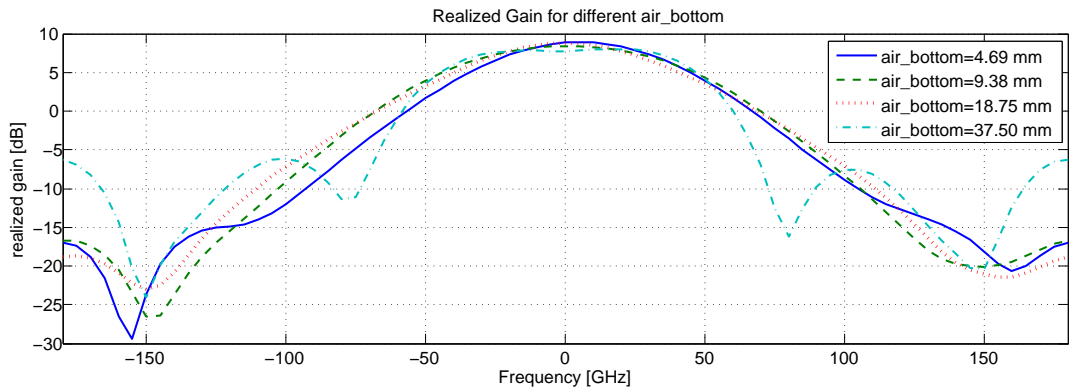
Figure 4.13: Parameter S11 (a) and the antenna pattern (b) with respect to the variation of the slot plane length (`subst.l`).

### 4.2.3 Reflector Parametrization

With an increase of the distance between the reflector and the antenna itself, the maximum gain in the main direction decreases slightly while the beam-width increases. For high values, the size of the reflector sheet is not sufficient and the side lobes are growing. As explained in Section 4.1.3, the reflector mainly influences the electric field radiated from the feeding structure. Therefore, a variation of the distance between the antenna and the reflector mainly influences the lower resonant frequency.



(a)



(b)

**Figure 4.14:** Parameter  $S_{11}$  (a) and the antenna pattern (b) in respect to the variation of  $air\_bottom$ .

The variation of the reflector sheet size causes a variation of the side-lobe levels (Figure 4.15). These effects can be explained with the non-ideal size reflector which causes diffracted field at its edges [18].

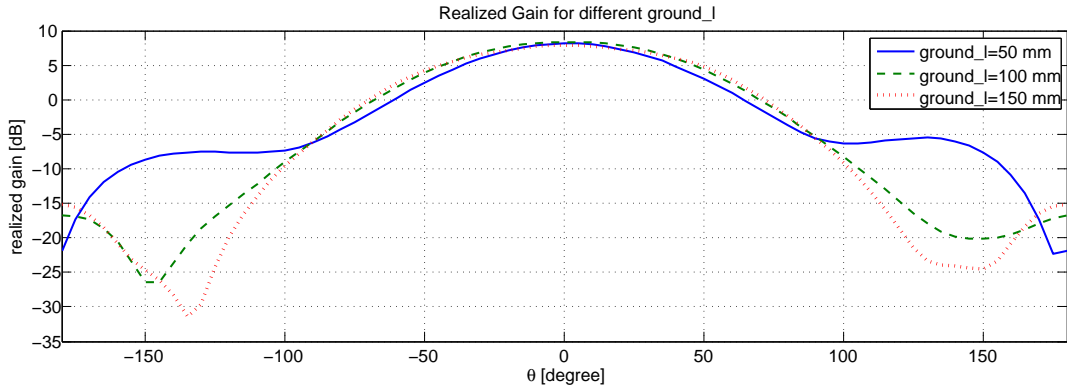


Figure 4.15: Antenna pattern in respect to the variation of `ground_l`.

### 4.3 Implementation

The final design was made using the parameter values of Table 4.1 and a RO4350B laminate produced by Rogers [19] with a relative dielectric constant of 3.66. According to the requirements (Section 1.2), the antenna has been designed for a center frequency of 4 GHz and an operating bandwidth (for the input impedance as well as for the pattern parameters) of a minimum of 500 MHz.

Parameter name	Parameter value
<code>air_bottom</code>	9.60 mm
<code>air_top</code>	8.80 mm
<code>feed_w</code>	2.50 mm
<code>ground_l</code>	100.00 mm
<code>patch_l</code>	20.00 mm
<code>slot_l</code>	14.70 mm
<code>slot_w</code>	0.50 mm
<code>stub1_l</code>	19.25 mm
<code>stub2_l</code>	4.80 mm
<code>subst_h</code>	1.524 mm
<code>subst_l</code>	50.00 mm

Table 4.1: Geometrical parameters of the final design.

### 4.3.1 Input Characteristics

The return-loss and the isolation between the two feeding ports (Figure 4.16) show a good performance over the frequency range. The two -10 dB corner frequencies are at 3.6 GHz and 4.6 GHz. This leads to an input bandwidth of 1 GHz around a center frequency of 4.1 GHz. The port isolation ( $S_{21}$ ) is beyond the -15 dB level for the whole frequency range. The return-loss and isolation of the second port have the same characteristics as those from the first port which are shown in Figure 4.16.

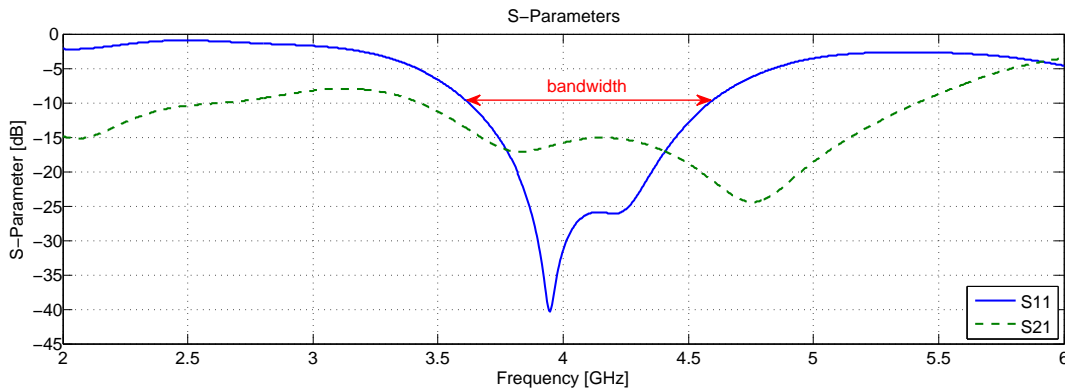


Figure 4.16: S-Parameters of the final design.

### 4.3.2 Radiation Patterns

The realized antenna gain (Figure 4.17) shows an absolute maximum of 8.7 dB in the main beam direction at  $\theta = -10^\circ$  and  $\phi = 0^\circ$ . The highest side-lobe is more than 20 dB smaller than the main-lobe. The 3 dB-beamwidth at 4.0 GHz is  $65.8^\circ$  in the xz-plane and  $71.9^\circ$  in yz-plane.

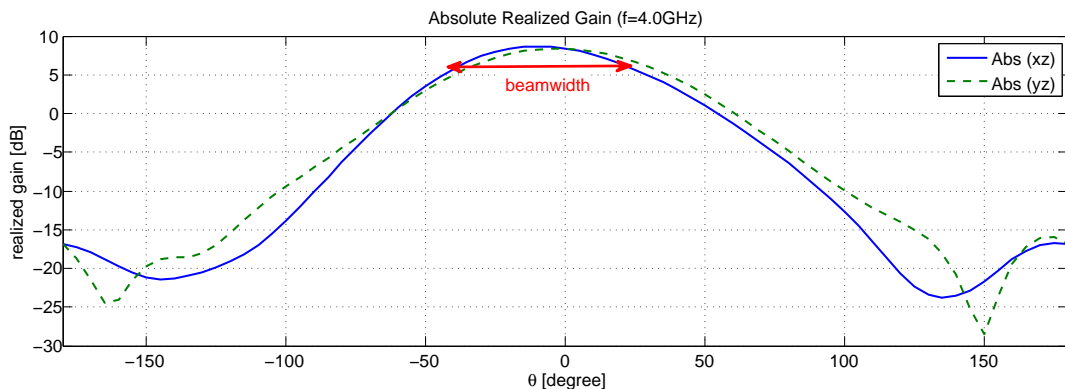
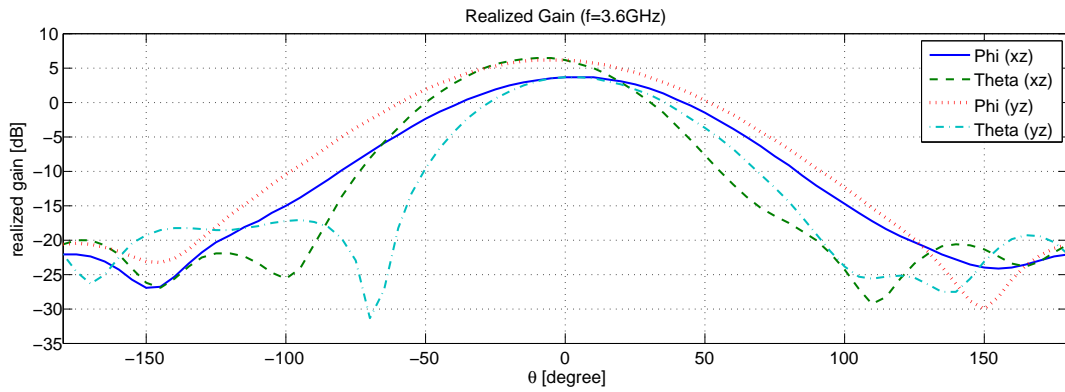
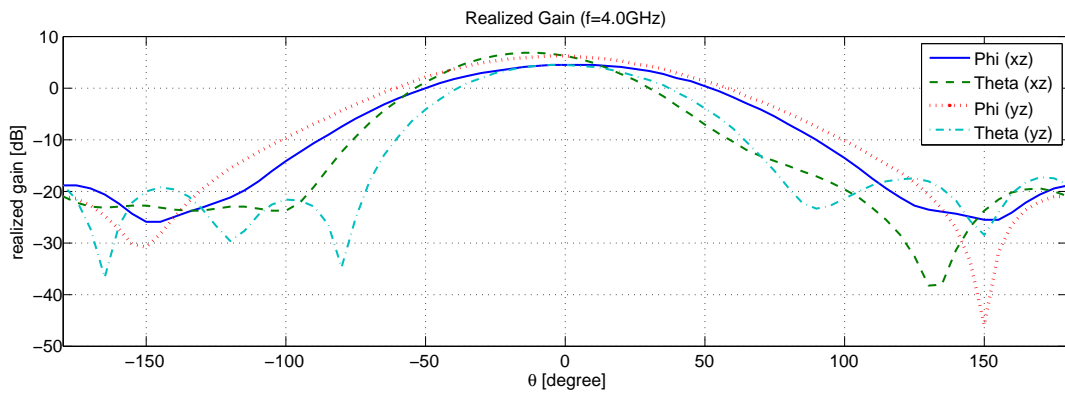


Figure 4.17: Absolute realized gain of the final design.

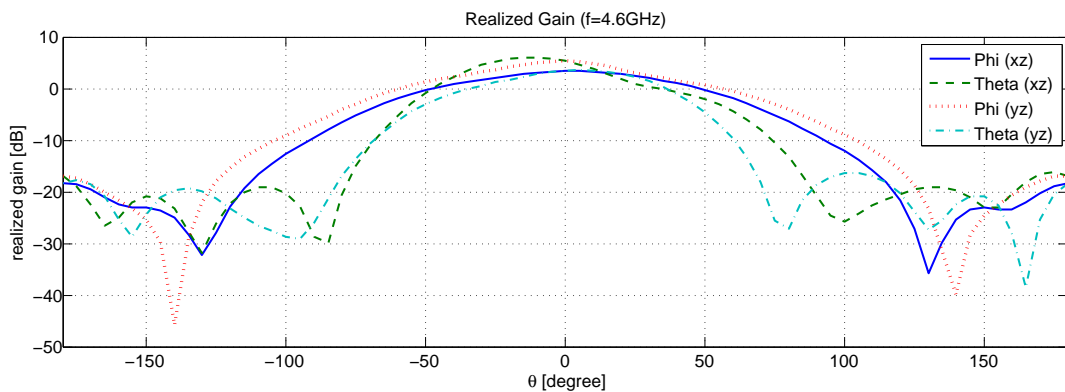
The two field components of the radiated wave show a maximum difference of 2 dB in the main direction (Figure 4.18). This difference varies slightly over the frequency and shows a minimum at the center frequency.



(a) 3.6 GHz



(b) 4.0 GHz



(c) 4.6 GHz

**Figure 4.18:** Realized gain for both field components of the final design.

In the main beam direction, the variation of the realized gain is roughly 1 dB over the operating frequency range. Also for other directions, the variation shows a stable behavior (Figure 4.19).

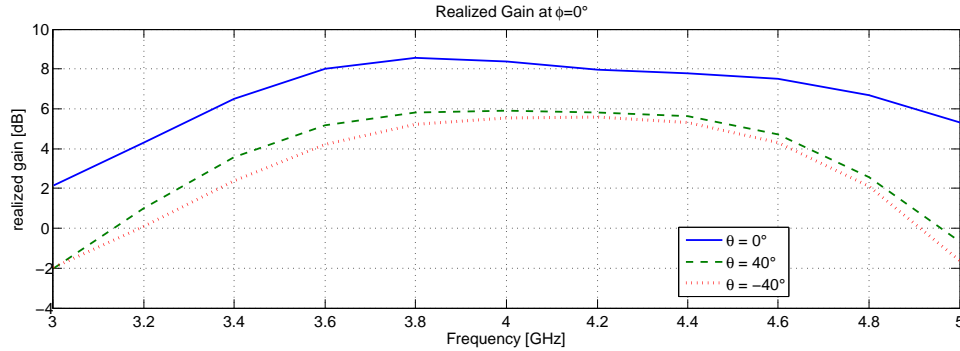
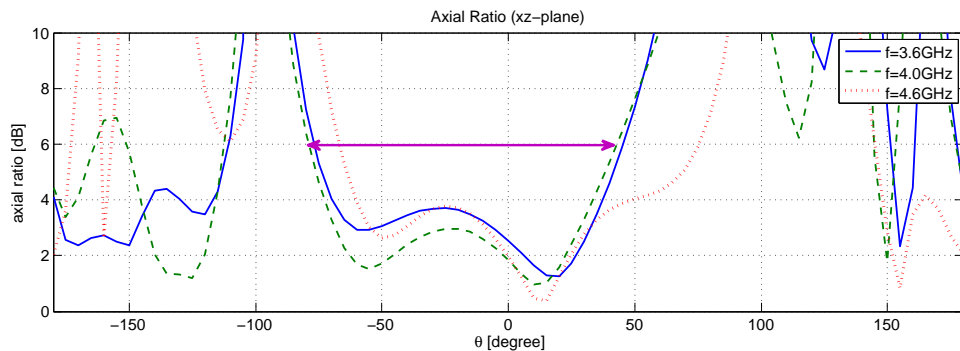
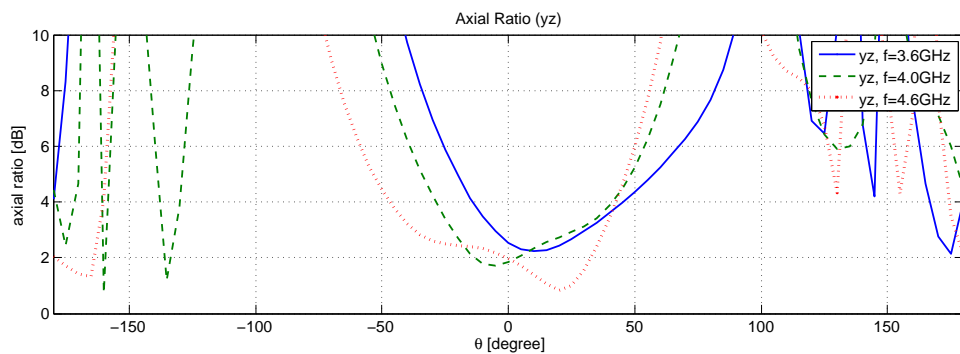


**Figure 4.19:** Absolute realized gain over the frequency of the final design.

In the  $xz$ -plane, the axial ratio has a 6dB-beamwidth of  $120^\circ$  at 4 GHz. In the  $yz$ -plane, the 6dB-beamwidth is  $95^\circ$ . For lower frequencies, the behavior of the axial ratio remains roughly the same, while for higher frequencies, the beamwidth increases.



(a)  $xz$ -plane



(b)  $yz$ -plane

**Figure 4.20:** Axial ratio of the final design.

### 4.3.3 UWB Characteristics

To simulate the UWB characteristics, two models of the patch antenna have been placed facing each other in a distance of 40 cm. One port of the transmitting antenna was excited with an impulse. The group delay for the copolarization and the impulse response were measured between the excited port and the complementary port (with the same polarization), while the group delay for the copolarization was measured using the second port of the receiving antenna.

The envelope of the impulse response (Figure 4.21) shows a width ( $\tau_{FWHM}$ ) of 0.67 ns and a 10% ringing of 2.01 ns.

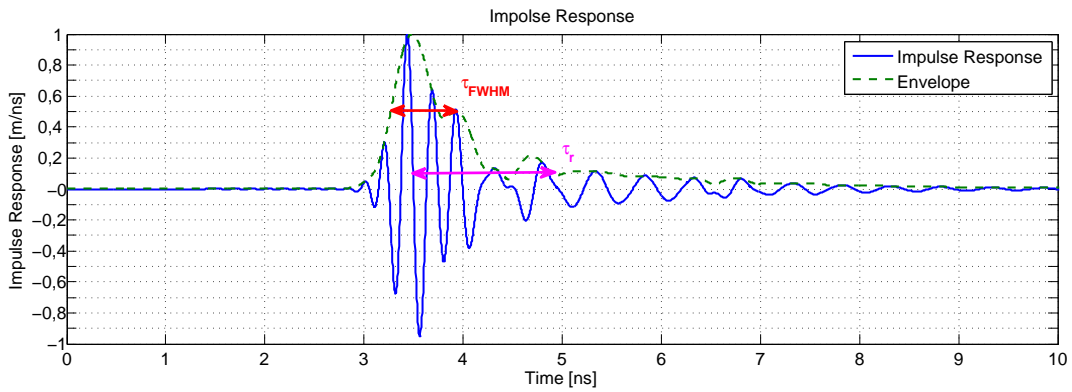


**Figure 4.21:** Impulse response of the final design.

The variation of the group delay around the mean value (1.61 ns) of the operating frequency band (Figure 4.22) is 0.15 ns for the copolarization. The variation of the crosspolarization is naturally much higher (0.6 ns).

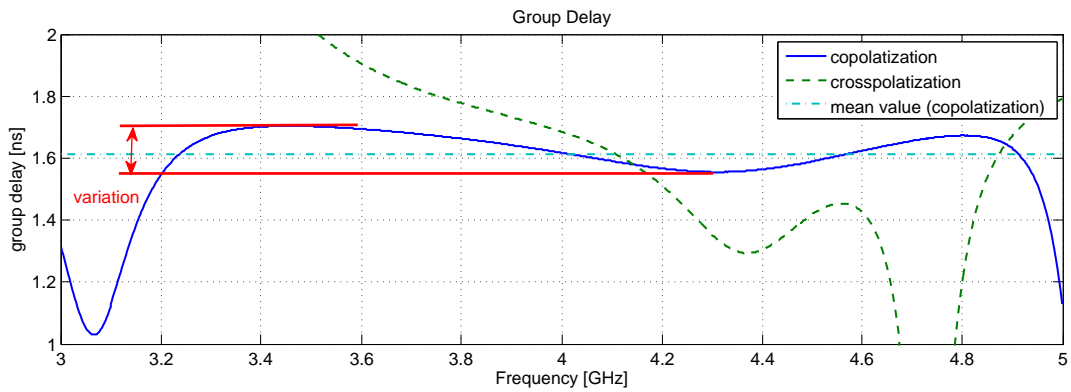


**Figure 4.22:** Group delay of the final design.

# 5 Implementation of the Antipodal Tapered-Slot Antenna

Additionally to the broad-side radiating patch antenna which has been presented in Chapter 4, an end-fire radiating antipodal tapered slot antenna already presented in [11] has been chosen to be implemented (Section 3.7).

## 5.1 Design Elements

The antenna design consists of five parts: a coplanar waveguide feed with a characteristic impedance of  $50\ \Omega$ , a transition between the coplanar waveguide and the substrate integrated waveguide (SIW), the substrate integrated waveguide itself, an antipodal linearly tapered slot antenna, and a dielectric rod (Figure 5.1).

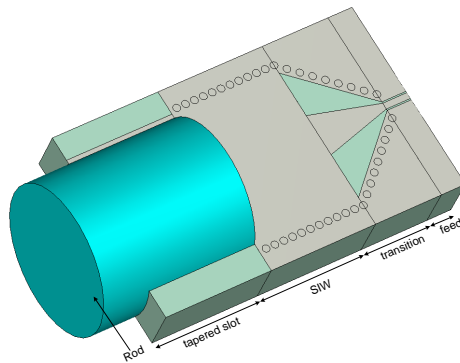


Figure 5.1: 3D model of the antipodal tapered slot antenna.

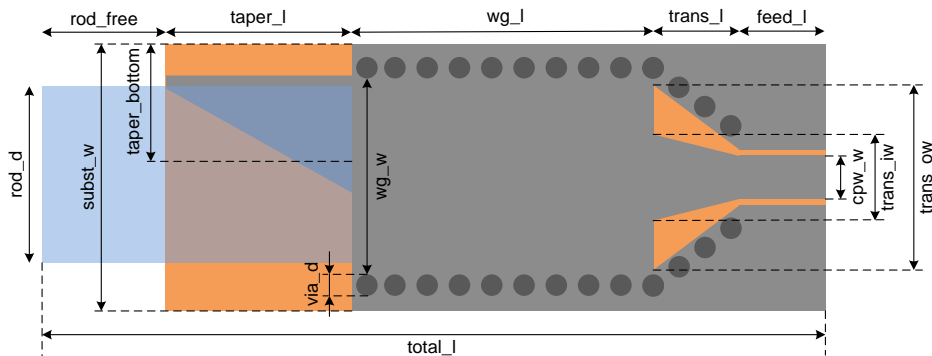
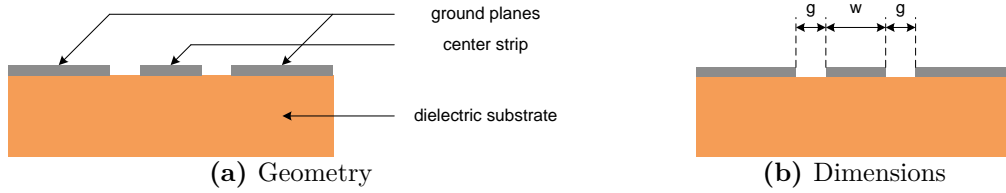


Figure 5.2: Geometry of the antipodal tapered slot antenna.

### 5.1.1 Coplanar Waveguide

Coplanar waveguides (CPW) consist of a metallic strip placed on a dielectric substrate with two adjacent and parallel ground electrodes placed on the same surface (Figure 5.3a) and have been first published in [20].

There are two main types of coplanar waveguides: the classical structure with central strip and coplanar grounds (CPW) and the cavity-backed or grounded coplanar waveguide (GCPW). The difference between CPW and GCPW lies in the mode that can be excited: the normal CPW line can support the dominant even mode (CPW-mode or even mode) or the slotline mode (odd mode), which is normally undesired. The odd mode is defined by electric force lines between the two coplanar grounds and can be shorted by means of air bridges; GCPWs can also support a microstrip mode, due to the presence of the back metal plane. Dimensions, frequencies and materials define the condition of existence for the undesired modes.



**Figure 5.3:** Geometry and dimensions of a CPW.

The characteristic impedance of a CPW can be calculated using Equation 5.1 and the parameters of Figure 5.3b [21].

$$Z_0 = \frac{\eta}{4\sqrt{\epsilon_e}} \frac{K'(k)}{K(k)} \quad (5.1)$$

where

$$k = \frac{w}{w + 2g}, \quad (5.2)$$

$$\epsilon_e = 1 + \frac{\epsilon_r - 1}{2} \frac{K'(k)}{K(k)} \frac{K(k_1)}{K'(k_1)}, \quad (5.3)$$

$$k_1 = \frac{\sinh\left(\frac{\pi w}{4h}\right)}{\sinh\left(\frac{\pi(w+2g)}{4h}\right)}. \quad (5.4)$$

with

$w$  = width of the central strip [mm]

$g$  = width of the gap between the central strip and the coplanar grounds [mm]

$K(k)$  = complete elliptical integral of first kind

$K'(k) = K(k')$

$k' = (1 - k^2)^{1/2}$

### 5.1.2 Substrate Integrated Waveguide

The concept of substrate integrated circuits is to synthesize a non-planar structures with a dielectric substrate and make it in a planar form. The synthesis can be achieved by using air holes to modify the profile of the dielectric constant and metalized via holes to replace continuous metallic walls [22].

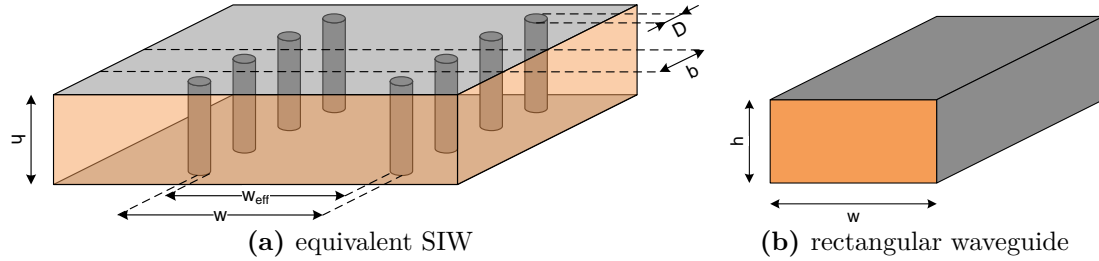


**Figure 5.4:** SIW and its equivalent rectangular waveguide [22].

In order to synthesize a rectangular waveguide (Figure 5.4b) two parallel rows of metalized via holes are fabricated into the substrate (Figure 5.4a). To ensure negligible leakage losses, two design rules should be considered:

$$b \leq 2D \quad (5.5)$$

$$D < \frac{\lambda_g}{5} \quad (5.6)$$

If properly designed, the losses can be neglected and the SIW can be modeled as a conventional rectangular waveguide on its dominant mode  $TE_{10}$  [22]. Due to the small height  $h$  compared to the width  $w_{eff}$ , SIWs support only  $TE_{n0}$  modes. Furthermore, the presence of gaps on the side walls inhibits the formation of any TM mode.

### 5.1.3 Transition

To excite the SIW with the desired waveguide mode ( $TE_{10}$ ), a transition between the CPW and the SIW as presented in [23] is used. In this transition (Figure 5.5) a quasi-microstrip line is connected to the SIW while its bottom ground plane is gradually removed. The quasi-microstripline is linearly tapered to the width of the feeding points (SIW and CPW).

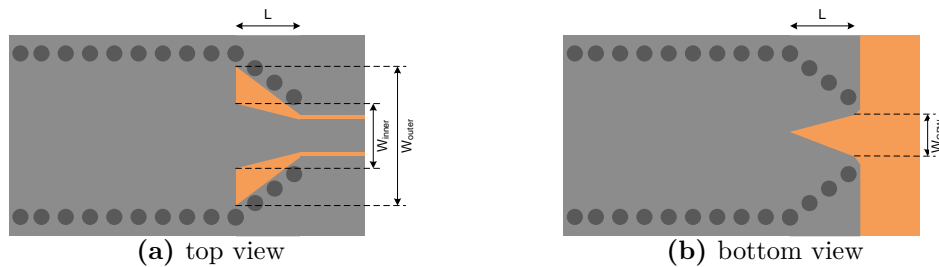


**Figure 5.5:** CPW to SIW transition.

### 5.1.4 Tapered Slot

Tapered Slot Antennas (TSA) are planar structures consisting of a gradual a transition from a printed line or a waveguide to the free space, that can be shaped very different profiles and offer a wide-band (up to 170%), linearly polarized (in the plane of the antenna), end-fire radiation with a directivity up to 10 dB at its maximum [24]. Contrary to conventional TSA, where the tapered slot is printed on one side of the dielectric substrate, antipodal TSA (ATSA) is printed on both faces of the substrate. For this design, an antipodal linear transition is used (Figure 5.6).

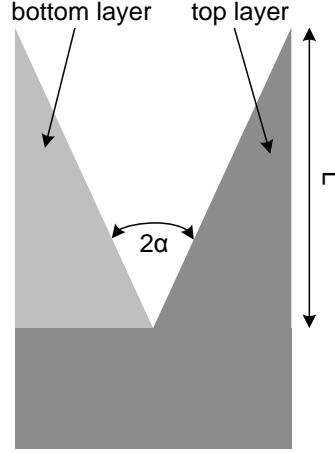


**Figure 5.6:** Geometry of an antipodal linearly tapered slot antenna.

For the design of an ALTSA two parameters are of interest: the length ( $L$ ) of the tapered slot and the flare angle ( $2\alpha$ ). For ATSA which are fed by a SIW, an overlap between the two metallic covers of the tapered slot can be used to match the input impedance to the characteristic impedance of the SIW [25].

### 5.1.5 Dielectric Rod

The dielectric rod can be seen as an imperfect guide for electromagnetic waves. In this design, the rod is fed by the antipodal linearly tapered slot. Together with the SIW, the ALTSA excites a  $TE_{11}$ -like mode in the dielectric rod. The mode excited in the circular dielectric waveguide is the responsible for a circularly polarized radiation from the rod aperture. To allow the radiation mechanism to take place, the diameter of the dielectric rod must be properly chosen to set the guided wavelength  $\lambda_G$  (Equation 5.7), associated to the desired mode  $TE_{11}$ , bigger then all wavelengths in the intended operating range.

$$\lambda_G \approx 0.58 \frac{\lambda}{\sqrt{\epsilon_r}} \quad (5.7)$$

The directivity of the dielectric rod antenna as well as the HPBW are depended on the length of the rod in free-space wavelengths ( $L_\lambda$ ):

$$D \approx 8L_\lambda \quad (5.8)$$

$$HPBW \approx \frac{60^\circ}{\sqrt{L_\lambda}} \quad (5.9)$$

## 5.2 Parametric Analysis of the Design Elements

In this Section, the effects of the variation of the design parameters of the antipodal tapered-slot antenna (Figure 5.1 and 5.2) on the input reflection ( $S_{11}$ ) and on the radiation pattern (in terms of realized gain on the xz-plane) are examined.

### 5.2.1 Coplanar Waveguide Parameterizations

The variation of the width of the middle strip of the CPW ( $cpw\_w$ ) causes a change of the characteristic impedance. However, since the return-loss of the antenna is always calculated with respect to the input impedance of the CPW, it does not change significantly for different widths of the middle strip of the CPW (Figure 5.7).

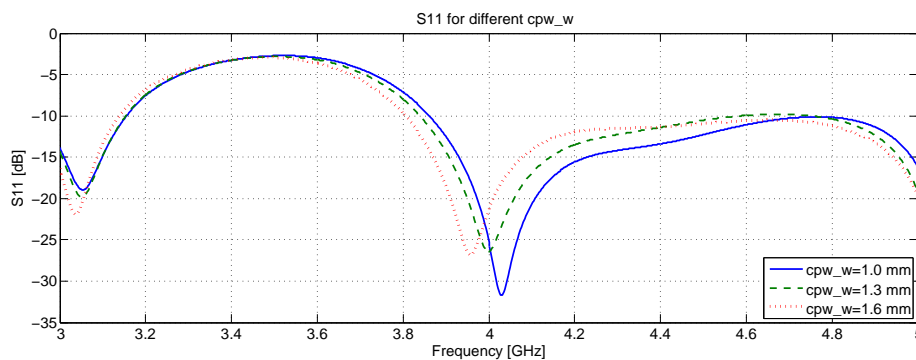


Figure 5.7: Input reflection coefficient with respect to the variation of  $cpw\_w$ .

### 5.2.2 Substrate Integrated Waveguide Parameterizations

An increase of the effective width of the SIW ( $wg\_w$ ) allows an excitation of the desired  $TE_{10}$  mode at lower frequencies. Since the variation of  $wg\_w$  also influences the geometry of the tapered slot, the main effect on the return-loss (Figure 5.8) is a shift to the left of the antennas pass-band for increasing values of  $wg\_w$ .

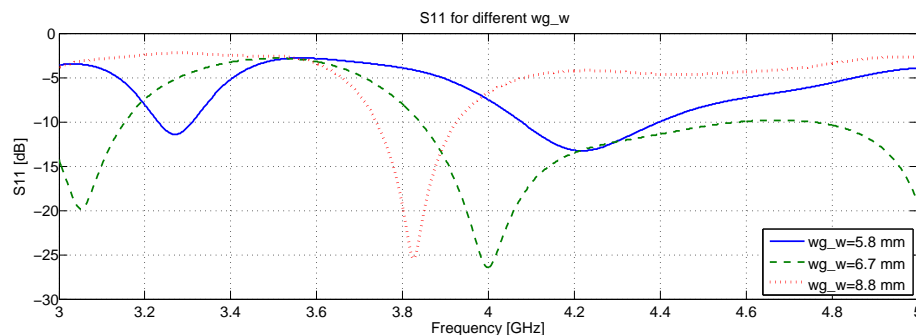
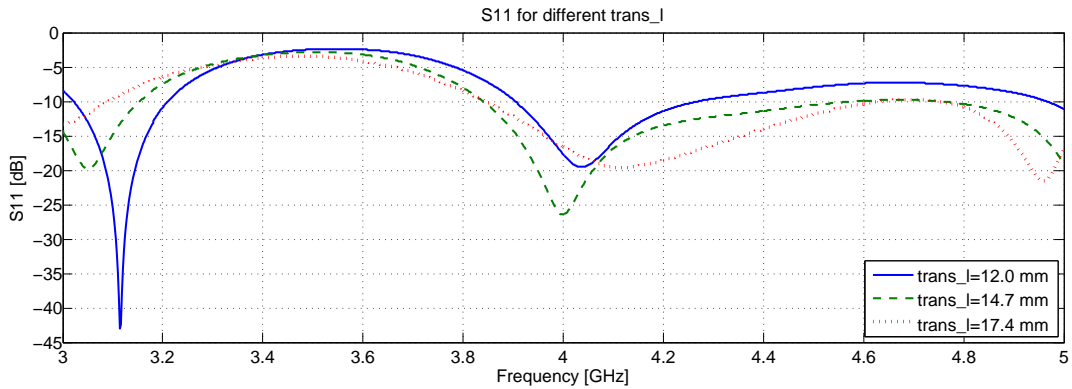


Figure 5.8: Input reflection coefficient with respect to the variation of  $wg\_w$ .

### 5.2.3 Transition Parameterizations

The variation of the length of the CPW-to-SIW transition ( $\text{trans}_l$ ) causes a change of the absolute matching (Figure 5.9). For higher values ( $\text{trans}_l \geq 14.7$  mm), the 10dB-bandwidth remains unchanged.



**Figure 5.9:** Input reflection coefficient with respect to the variation of  $\text{trans}_l$ .

Similar to the variation of  $\text{trans}_l$ , the alteration of the quasi-microstrip ( $\text{trans}_{iw}$ ) has an impact on the absolute matching (Figure 5.10). Differently to the afore mentioned variation, the 10dB-bandwidth is not changing.

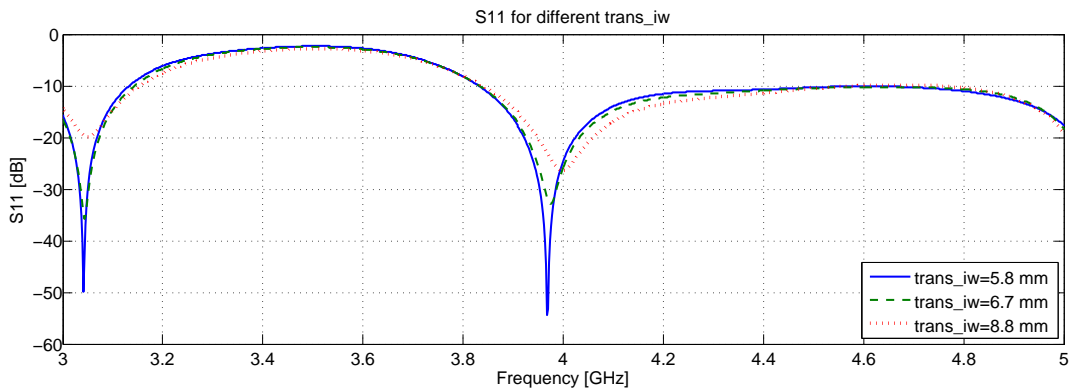


**Figure 5.10:** Input reflection coefficient with respect to the variation of  $\text{trans}_{iw}$ .

### 5.2.4 Tapered Slot Parameterizations

The length of the tapered slot (`taper_l`) influences mainly the cutoff frequency of the operating frequency range (Figure 5.11). Since the variation of `taper_l` also influences the flare angle of the tapered slot, a change of the behavior of the axial ratio can be noticed.

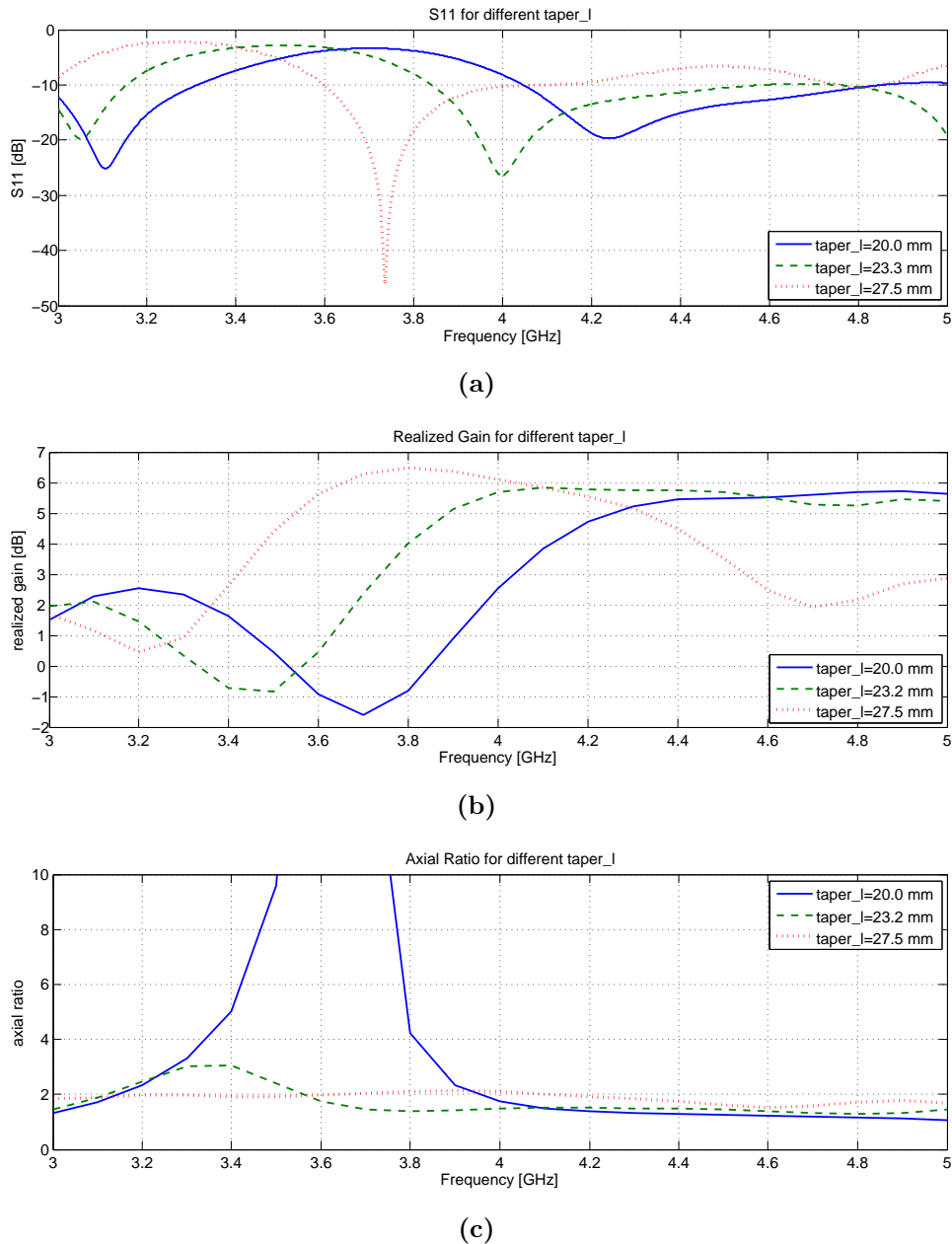


**Figure 5.11:** Parameter S11 (a), realized gain (b) and axial ratio (c), with respect to the variation of `taper_l`.

Similar to the alteration of `trans_1`, the bottom width of the tapered slot influences the flare angle. For steep angles (`taper_1` = 12.5 mm), the behavior of the axial ratio significantly impairs (Figure 5.12).

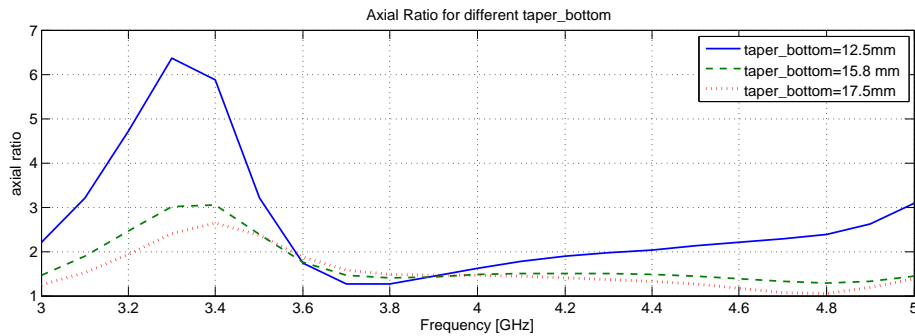
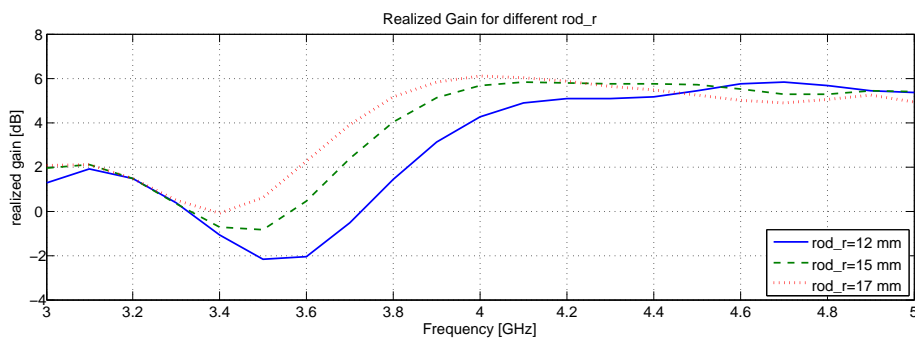


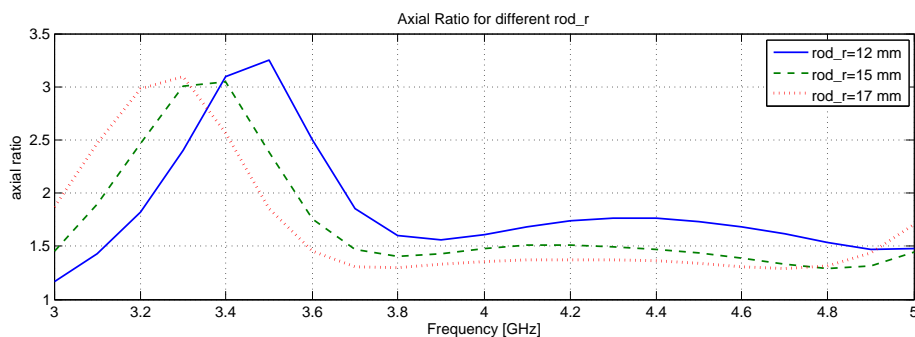
Figure 5.12: Axial ratio with respect to the variation of `taper_bottom`.

### 5.2.5 Dielectric Rod Parameterizations

The radius of the dielectric rod (`rod_r`) determines the cutoff frequency for the  $TE_{11}$  in the rod itself. A variation of this parameter causes a shift of the realized gain and the axial ratio in the frequency domain (Figure 5.13).



(a)

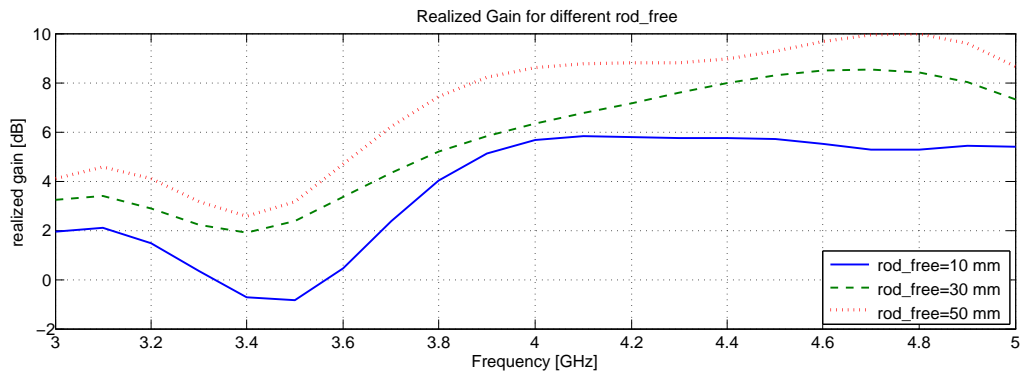


(b)

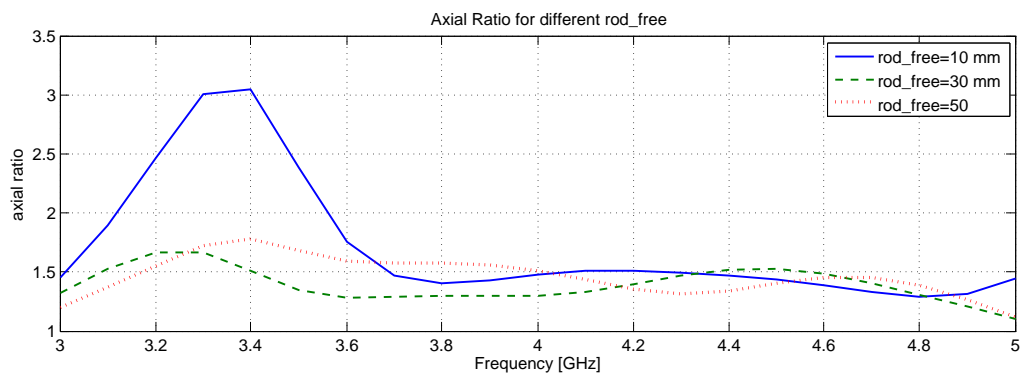
Figure 5.13: Parameter realized gain (a) and axial ratio (b) with respect to the variation of `rod_r`.

The alteration of the length of the dielectric rod (`rod_free`) increases the absolute realized gain in the main beam direction, as well as the bandwidth of the axial ratio (Figure 5.14).

At 4 GHz, the radiation pattern of the antenna shows an increase of the realized gain in the main beam direction and a narrowing of the HPBW (Figure 5.15).



(a)



(b)

**Figure 5.14:** Parameter realized gain (a) and axial ratio (b) with respect to the variation of `rod_free`.

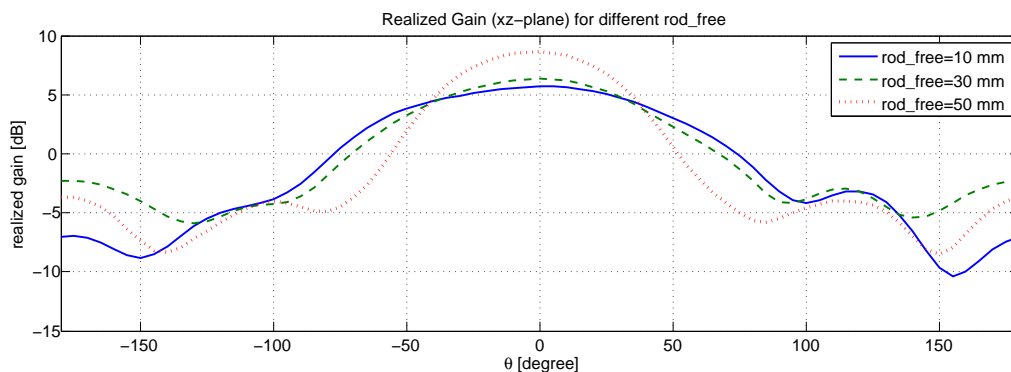


**Figure 5.15:** Antenna pattern with respect to the variation of `rod_free`.

### 5.3 Implementation

The final design was made using a Rogerst RT/duroid 6006 laminate [26] with a relative dielectric constant of  $\epsilon_r = 6.15$ . The rod was fabricated with a Mullite porcelain with a dielectric constant of  $\epsilon_r = 6$ . Since the chosen substrate is not available in the needed thickness of 10 mm, 4 layers of 2.5 mm thick substrate have been stacked.

The geometrical parameters for the model in Figure 5.2 which have been used for the final design, are listed in Table 5.1.

Parameter name	Parameter value	Parameter name	Parameter value
cpw_g	0.30 mm	taper_l	23.20 mm
cpw_w	1.30 mm	taper_top	1.30 mm
feed_l	5.40 mm	trans_iw	8.80 mm
rod_free	10.00 mm	trans_l	14.70 mm
rod_r	15.00 mm	via_d	1.50 mm
subst_h	10.00 mm	wg_l	23.10 mm
subst_w	40.00 mm	wg_w	30.00 mm
taper_bottom	15.80 mm	total_	76.40 mm

Table 5.1: Geometrical parameters of the final design.

#### 5.3.1 Input Characteristics

The return-loss of the antipodal tapered slot antenna has a 10dB-bandwidth of 760 MHz at a center frequency of 4.2 GHz (Figure 5.16). The trade-off between the initial requirements and the final results has been made due to the manufacturing process which has only made available certain values for the thickness of the substrate. The optimal matching is at a frequency of 4 GHz where the return-loss is -26.5 dB.

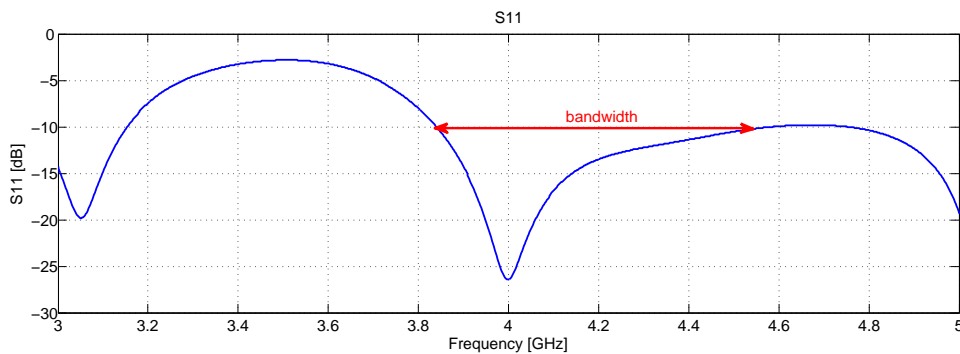
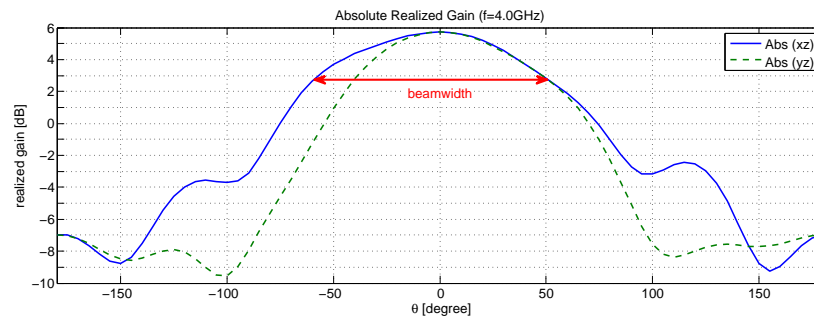


Figure 5.16: S-Parameters of the final design.

### 5.3.2 Radiation Patterns

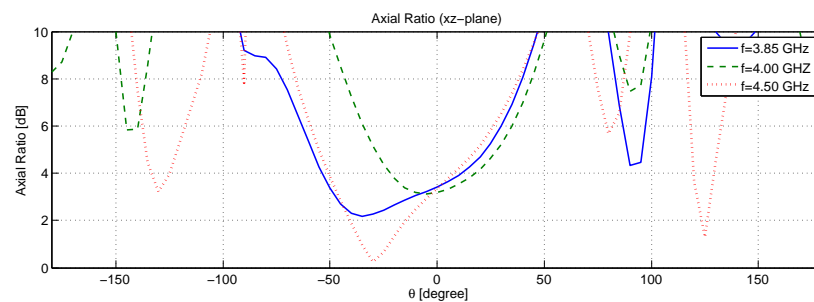
The absolute realized gain at a frequency of 4 GHz (Figure 5.17) shows a maximum of 5.7 dB and a HPBW of  $110^\circ$  in the  $xz$ -plane and  $90^\circ$  in the  $yz$ -plane. The side-lobe level is 8 dB and the back-lobe is 12 dB smaller than the main lobe. These values are not optimal, but consonant with the original design which has been presented in 3.6.



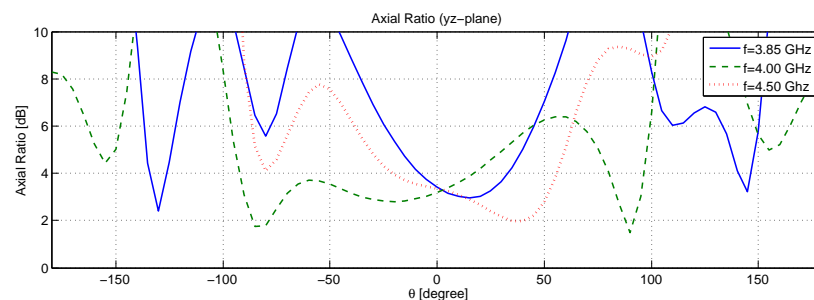
**Figure 5.17:** Absolute realized gain of the final design.

The orthogonal components of the radiated field (Figure 5.19) show a difference of 3dB in the main beam direction, which is acceptable for an axial ratio of less than 6 dB. While the Phi-component of the  $xz$ -plane has a minimum at 4 GHz, the Theta-component has its minimum at 3.85 GHz and shows a more stable behavior for the higher frequencies.

As already indicated in Figure 5.19, the axial ratio of the antipodal tapered slot antenna (Figure 5.18) shows a sufficient behavior in the main beam direction. The beamwidth for an acceptable axial ratio of less than 6 dB varies over the frequency. In the  $xz$ -plane the minimal beamwidth is  $70^\circ$  at 4 GHz, while in the  $yz$ -plane, the minimum is  $70^\circ$  at 3.85 GHz.

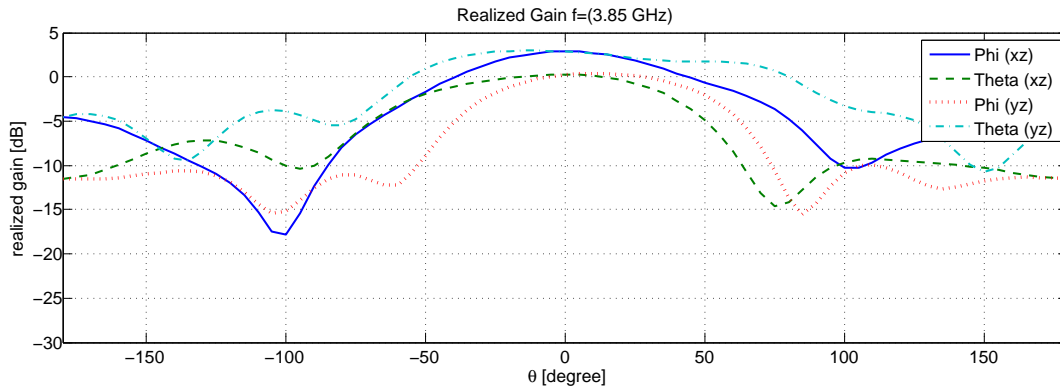


(a)  $xz$ -plane

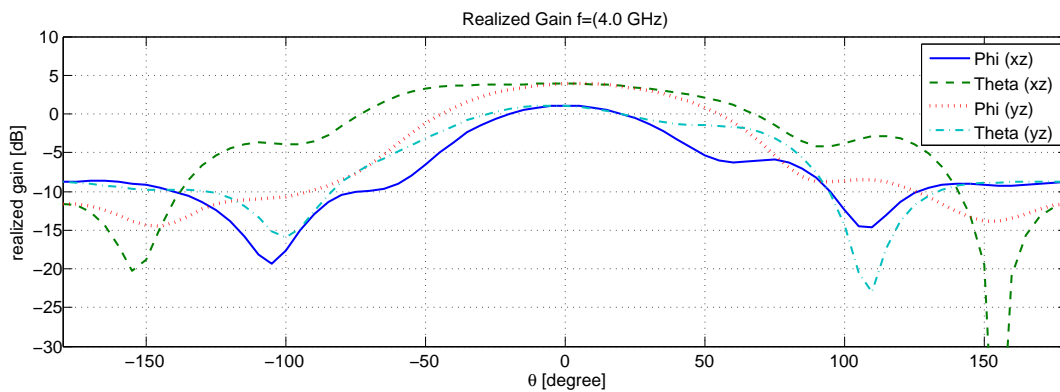


(b)  $yz$ -plane

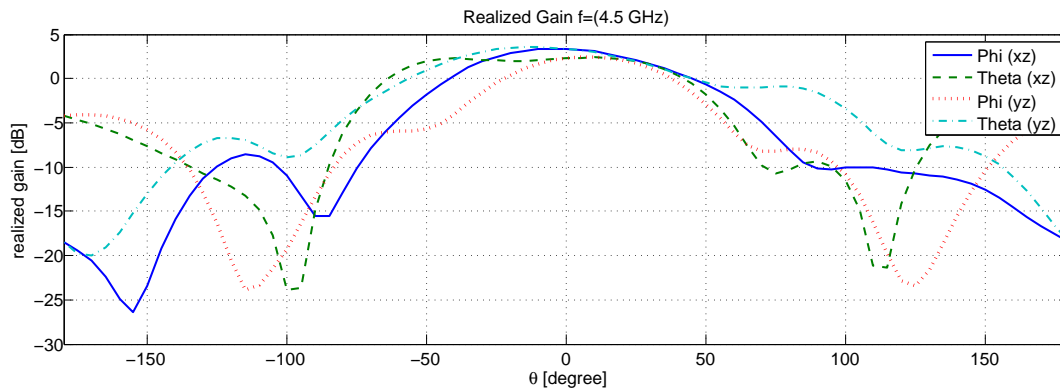
**Figure 5.18:** Axial ratio pattern of the final design.



(a) 3.85 GHz



(b) 4.00 GHz



(c) 4.50 GHz

**Figure 5.19:** Realized gain for both field components of the final design.

Over the frequency, the realized gain in the main beam direction shows a constant behavior starting from 4 GHz (Figure 5.20). However the drop of the absolute value of the realized gain at 3.8 GHz is still in the acceptable range of 3 dB. The axial ratio in the main beam direction shows a good behavior over the frequency and stays beyond the limit of 2 starting from 3.7 GHz.

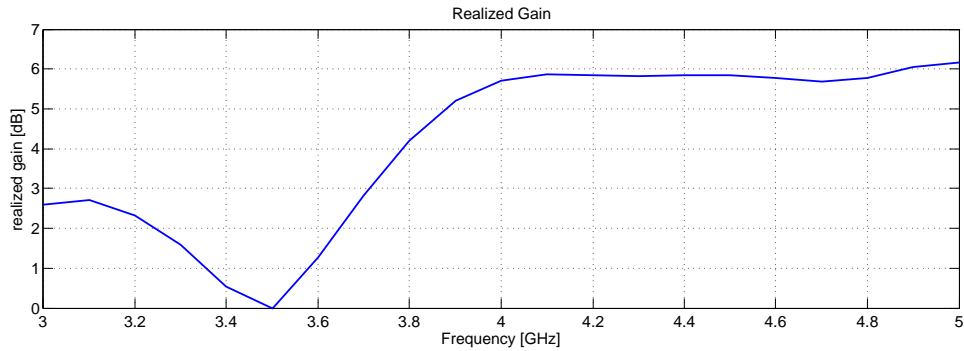


**Figure 5.20:** Realized gain in the main beam direction of the final design.

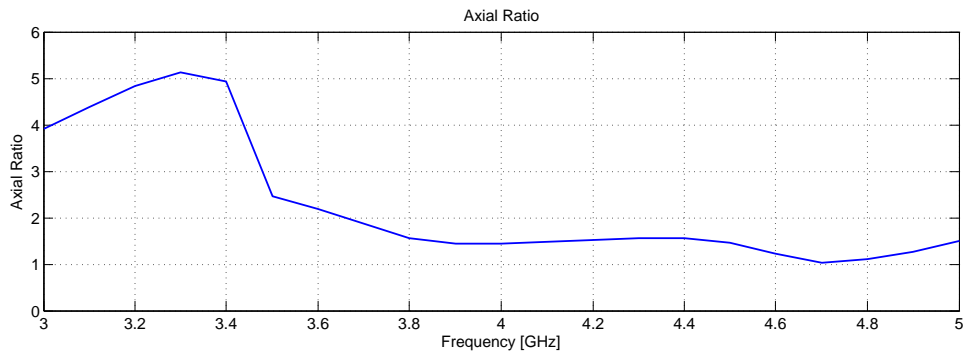


**Figure 5.21:** Axial ratio in the main beam direction of the final design.

### 5.3.3 UWB Characteristics

The UWB characteristics of the antipodal tapered slot antenna have been simulated. Since this antenna has only one feeding port, the group delay cross-polarization was not extracted in this case.

The envelope of the impulse response (Figure 5.22) shows a width of ( $\tau_{FWHM}$ ) 0.91 ns and a 10% ringing of 3.4 ns for an evaluated frequency range of 3–5 GHz.

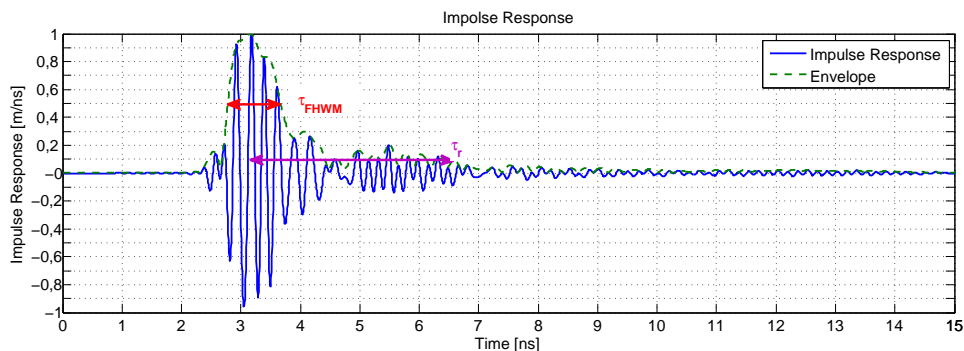


**Figure 5.22:** Impulse response of the final design.

The variation of the group delay (Figure 5.23) around the mean value (1.01 ns) between the corner frequencies (3.8 GHz and 4.6 GHz) is 0.15 ns. Such values show a low distortion of the transmitted and received pulse in the operating frequency range.

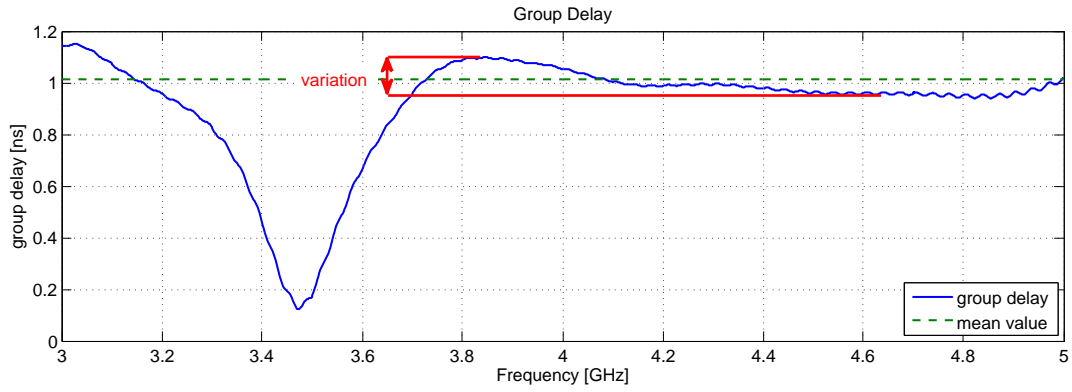


**Figure 5.23:** Group delay of the final design.

## 6 Conclusion and Prospects

In this work, a dual and a circular polarized ultra-wide band antenna design for automotive applications have been developed and characterized relatively to their UWB performance, in terms of gain, matching and dispersion, as well as their overall geometrical dimensions. Due to the future application of the antennas, the time domain characteristics, such as impulse response and group delay, were the main focus area of the design process. To ease up the development of the mobile counterpart, and to comply with the European standards, antenna designs able to transmit circular or dual polarized waves have been chosen.

### 6.1 Results

The simulated results show a satisfactory UWB performances, as reported in (Table 6.1).

Characteristic	Patch	Tapered Slot
Dimensions [mm <sup>3</sup> ]	50 × 50 × 21.5	40 × 76.4 × 30
Relative dielectric constant	3.66	6.15
Center frequency [GHz]	4.10	4.20
Operating frequency range [GHz]	3.60–4.60	3.84–4.55
Return-loss bandwidth [MHz]	1600	760
Gain bandwidth [MHz]	1635	> 1500
Axial ratio bandwidth [MHz]	n.A.	> 1500
HPBW (@4 GHz) [degree]	71.9	91.3
Maximal realized gain (@4 GHz) [dB]	8.7	5.7
Width of the impulse response envelope [ns]	0.67	0.91
Variation of the group delay [ns]	0.15	0.15

**Table 6.1:** Characteristics of the two antenna designs.

The required minimum bandwidth of 500 MHz is reached by both designs. To increase the return-loss bandwidth of the tapered slot antenna, a new design with an increased width of the SIW can be taken into consideration.

Due to the limits of CST Microwave Studio, the axial ratio bandwidth could not be simulated. During the simulations of the tapered slot antenna, no upper corner frequency for the gain bandwidth nor for the axial ratio bandwidth could be found.

Compared to the smallest wavelength, the height of the patch antenna is not negligible. Therefore, materials with higher relative permittivity can be used in place of the air slabs, in order to reduce the overall thickness. To minimize the microstrip and slot dimensions, a further material with high permittivity can be employed. However, this approaches will negatively influence the bandwidth characteristics as well as the manufacturing costs.

As for the tapered slot antenna, using a material with relative permittivity higher than 6, will dramatically reduce its radiation efficiency. The material used in this work to implement the TSA was chosen because it offers a reasonable trade-off between radiation efficiency, bandwidth, and antenna dimensions.

The verification of these parameters through measurements of the manufactured prototypes are currently being developed and will be presented in a forthcoming appendix.

## 6.2 Future Work

The linearly-polarized UWB antennas for the aforementioned mobile counterpart will be designed in an upcoming thesis. The main task will be to reduce the antenna dimensions and optimize the structure for receiving a circular polarized wave, independently from the position of the stationary source of the incoming signal.

## List of Figures

2.1	Thevenin equivalent circuit and reference terminals and losses of an antenna . . . . .	4
2.2	Main beam aperture and radiation lobes . . . . .	5
2.3	Rotation of an electromagnetic wave and its polarization ellipse . . . . .	7
2.4	Input impedance bandwidth . . . . .	7
2.5	Impulse response and envelope . . . . .	8
2.6	Impulse response and envelope . . . . .	9
3.1	Alignment of simulated models and their far-field . . . . .	10
3.2	Geometry of the slot antenna . . . . .	11
3.3	Realized gain of the slot antenna . . . . .	12
3.4	$S_{11}$ of the slot antenna over the frequency . . . . .	13
3.5	Axial ratio of the slot antenna over the frequency . . . . .	13
3.6	Geometry of the probe antenna . . . . .	14
3.7	Realized gain of the probe antenna . . . . .	15
3.8	$S_{11}$ of the probe antenna over the frequency . . . . .	16
3.9	Axial ratio of the probe antenna over the frequency . . . . .	16
3.10	Geometry of the slot/strip loop antenna . . . . .	17
3.11	Realized gain of the loop antenna . . . . .	18
3.12	$S_{11}$ of the loop antenna over the frequency . . . . .	19
3.13	Axial ratio of the loop antenna over the frequency . . . . .	19
3.14	Geometry of the patch antenna . . . . .	20
3.15	Realized gain of the circularly fed patch antenna . . . . .	21
3.16	$S_{11}$ of the patch antenna over the frequency . . . . .	22
3.17	Axial ratio of the patch antenna at different frequencies . . . . .	22
3.18	Geometry of the tapered slot antenna . . . . .	23
3.19	Realized gain of the antipodal tapered slot antenna . . . . .	24
3.20	$S_{11}$ of the antipodal tapered slot antenna over the frequency . . . . .	25
3.21	Axial ratio of the antipodal tapered slot antenna . . . . .	25
4.1	Stack up of the dual-polarized patch antenna . . . . .	28
4.2	Geometries of the two layers of the dual-polarized patch antenna . . . . .	29
4.3	Stack-up and Geometry of a simple rectangular patch antenna . . . . .	30
4.4	Rectangular patch antenna and its equivalent cavity model . . . . .	30
4.5	Field configurations (modes) for a simple patch . . . . .	31
4.6	Aperture coupled feed . . . . .	31
4.7	Antenna with a flat reflector and gain for different distances . . . . .	32
4.8	$S_{11}$ with respect to the variation of the patch length ( <code>patch_1</code> ) . . . . .	33

4.9	S11 with respect to the variation of the patch height ( <code>air_top</code> ) . . . . .	33
4.10	S11 with respect to the variation of <code>slot_l</code> . . . . .	34
4.11	S11 with respect to the variation of <code>feed_w</code> . . . . .	34
4.12	S11 with respect to the variation of <code>stub2_l</code> . . . . .	35
4.13	Parameter S11 (a) and the antenna pattern (b) with respect to the variation of the slot plane length ( <code>subst_l</code> ) . . . . .	35
4.14	Parameter S11 (a) and the antenna pattern (b) in respect to the variation of <code>air_bottom</code> . . . . .	36
4.15	Antenna pattern in respect to the variation of <code>ground_l</code> . . . . .	37
4.16	S-Parameters of the final design . . . . .	38
4.17	Absolute realized gain of the final design . . . . .	38
4.18	Realized gain for both field components of the final design . . . . .	39
4.19	Absolute realized gain over the frequency of the final design . . . . .	40
4.20	Axial ratio of the final design . . . . .	40
4.21	Impulse response of the final design . . . . .	41
4.22	Group delay of the final design . . . . .	41
5.1	3D model of the antipodal tapered slot antenna . . . . .	42
5.2	Geometry of the antipodal tapered slot antenna . . . . .	42
5.3	Geometry and dimensions of a CPW . . . . .	43
5.4	SIW and its equivalent rectangular waveguide . . . . .	44
5.5	CPW to SIW transition . . . . .	44
5.6	Geometry of an antipodal linearly tapered slot antenna . . . . .	45
5.7	Input reflection coefficient with respect to the variation of <code>cpw_w</code> . . . . .	46
5.8	Input reflection coefficient with respect to the variation of <code>wg_w</code> . . . . .	46
5.9	Input reflection coefficient with respect to the variation of <code>trans_l</code> . . . . .	47
5.10	Input reflection coefficient with respect to the variation of <code>trans_iw</code> . . . . .	47
5.11	Parameter S11 (a), realized gain (b) and axial ratio (c), with respect to the variation of <code>taper_l</code> . . . . .	48
5.12	Axial ratio with respect to the variation of <code>taper_bottom</code> . . . . .	49
5.13	Parameter realized gain (a) and axial ratio (b) with respect to the variation of <code>rod_r</code> . . . . .	49
5.14	Parameter realized gain (a) and axial ratio (b) with respect to the variation of <code>rod_free</code> . . . . .	50
5.15	Antenna pattern with respect to the variation of <code>rod_free</code> . . . . .	50
5.16	S-Parameters of the final design . . . . .	51
5.17	Absolute realized gain of the final design . . . . .	52
5.18	Axial ratio pattern of the final design . . . . .	52
5.19	Realized gain for both field components of the final design . . . . .	53
5.20	Realized gain in the main beam direction of the final design . . . . .	54
5.21	Axial ratio in the main beam direction of the final design . . . . .	54
5.22	Impulse response of the final design . . . . .	54
5.23	Group delay of the final design . . . . .	55

# List of Tables

1.1	Basic requirements . . . . .	1
3.1	Comparison of circular and dual polarized broadband antennas . . . . .	26
3.2	Advantages and disadvantages of the recommended antenna designs . . . . .	27
4.1	Geometrical parameters of the final design . . . . .	37
5.1	Geometrical parameters of the final design . . . . .	51
6.1	Characteristics of the two antenna designs . . . . .	56

## Acronyms and Abbreviations

ALTSA	antipodal linearly tapered slot antenna
ATSA	antipodal tapered slot antenna
CP	circularly polarized
CPW	coplanar waveguide
FNBW	first-null beamwidth
FWHM	full width at half maximum
GCPW	grounded coplanar waveguide
HPBW	half-power beamwidth
LHCP	left-hand circularly polarized
Phi, Theta	orthogonal components of the electric farfield
RHCP	right-hand circularly polarized
$S_{11}$ , $S_{11}$	input reflection coefficient
SIW	substrate integrated waveguide
TSA	tapered slot antenna
UWB	ultra wide-band

# Bibliography

- [1] M. J. Copps and K. J. Martin, “First report and order 02-48,” Federal Communications Commission, Washington, D.C, Tech. Rep., 2002.
- [2] C. A. Balanis, *Antenna Theory: Analysis And Design, 3Rd Ed.* BWSTM, 2009.
- [3] “IEEE standard definitions of terms for antennas.” *IEEE Std 145-1993*, 1993.
- [4] Wikipedia, The Free Encyclopedia, “Circular polarization,” [http://en.wikipedia.org/wiki/File:Circular.Polarization.Circularly.Polarized.Light\\_With.Components\\_Right.Handed.svg](http://en.wikipedia.org/wiki/File:Circular.Polarization.Circularly.Polarized.Light_With.Components_Right.Handed.svg), 2013, [Online; accessed 02-January-2013].
- [5] W. Wiesbeck, G. Adamiuk, and C. Sturm, “Basic properties and design principles of uwb antennas,” *Proceedings of the IEEE*, vol. 97, no. 2, pp. 372–385, feb. 2009.
- [6] CST – Computer Simulation Technology AG, “CST Microwave Studio,” <http://www.cst.com/>.
- [7] J.-Y. Sze, K.-L. Wong, and C.-C. Huang, “Coplanar waveguide-fed square slot antenna for broadband circularly polarized radiation,” *Antennas and Propagation, IEEE Transactions on*, vol. 51, no. 8, pp. 2141 – 2144, August 2003.
- [8] Y. Muramoto and T. Fukusako, “Circularly polarized broadband antenna with l-shaped probe and l-shaped wide-slot,” in *Microwave Conference, 2007. APMC 2007. Asia-Pacific*, December 2007, pp. 1 –4.
- [9] B. Pan, R. Li, J. Papapolymerou, J. Laskar, and M. Tentzeris, “A cavity-backed broadband circularly polarized slot/strip loop antenna with a simple feeding structure,” in *Antennas and Propagation Society International Symposium 2006, IEEE*, July 2006, pp. 2595 –2598.
- [10] C. Yaping, S. Houjun, and L. Xin, “Design of a broadband wide-angle circularly polarized microstrip patch antenna with small phase deviation,” in *Microwave and Millimeter Wave Technology, 2008. ICMWT 2008. International Conference on*, vol. 3, April 2008, pp. 1089 –1091.
- [11] L. Song, A. Elsherbini, Y. Songnan, A. Fathy, A. Kamel, and H. Elhennawy, “Experimental development of a circularly polarized antipodal tapered slot antenna using siw feed printed on thick substrate,” in *Antennas and Propagation Society International Symposium, 2007 IEEE*, June 2007, pp. 1533 – 1536.
- [12] K. Carver and J. Mink, “Microstrip antenna technology,” *Antennas and Propagation, IEEE Transactions on*, vol. 29, no. 1, pp. 2 – 24, jan 1981.
- [13] H. Oltman and D. Huebner, “Electromagnetically coupled microstrip dipoles,” *Antennas and Propagation, IEEE Transactions on*, vol. 29, no. 1, pp. 151 – 157, jan 1981.
- [14] P. Katehi and N. Alexopoulos, “On the modeling of electromagnetically coupled microstrip antennas—the printed strip dipole,” *Antennas and Propagation, IEEE Transactions on*, vol. 32, no. 11, pp. 1179 – 1186, nov 1984.

- [15] D. Pozar, "Microstrip antenna aperture-coupled to a microstripline," *Electronics Letters*, vol. 21, no. 2, pp. 49–50, 17 1985.
- [16] R. Caso, A. Serra, M. Pino-Rodriguez, P. Nepa, and G. Manara, "A square ring slot feeding technique for dual-polarized patch antennas," in *Antennas and Propagation Society International Symposium, 2009. APSURSI '09. IEEE*, june 2009, pp. 1–4.
- [17] D. Pozar, "Microstrip antennas," *Proceedings of the IEEE*, vol. 80, no. 1, pp. 79–91, jan 1992.
- [18] J. D. Kraus, *Antennas*, 3rd ed. Mcgraw Hill Higher Education, 12 2001.
- [19] Rogers Corporation, "RO4000® Series - Data-Sheet," <http://www.rogerscorp.com/documents/726/acm/RO4000-Laminates---Data-sheet.pdf>.
- [20] C. Wen, "Coplanar waveguide: A surface strip transmission line suitable for nonreciprocal gyromagnetic device applications," *Microwave Theory and Techniques, IEEE Transactions on*, vol. 17, no. 12, pp. 1087–1090, dec 1969.
- [21] T. H. Lee, *Planar Microwave Engineering - A Practical Guide to Theory, Measurement, and Circuits*, har/cdr ed. Cambridge: Cambridge University Press, 2004.
- [22] K. Wu, D. Deslandes, and Y. Cassivi, "The substrate integrated circuits - a new concept for high-frequency electronics and optoelectronics," in *Telecommunications in Modern Satellite, Cable and Broadcasting Service, 2003. TELSIKS 2003. 6th International Conference on*, vol. 1, oct. 2003, pp. P–III–P–X vol.1.
- [23] F. Taringou and J. Bornemann, "New substrate-integrated to coplanar waveguide transition," in *Microwave Conference (EuMC), 2011 41st European*, oct. 2011, pp. 428–431.
- [24] X. Begaud, *Ultra Wide Band Antennas*, X. Begaud, Ed. ISTE Ltd., 2011.
- [25] Z. C. Hao, W. Hong, J. X. Chen, X. P. Chen, and K. Wu, "A novel feeding technique for antipodal linearly tapered slot antenna array," in *Microwave Symposium Digest, 2005 IEEE MTT-S International*, june 2005, p. 3 pp.
- [26] Rogers Corporation, "RT/duroid® 6006/6010 laminate data sheet," <http://www.rogerscorp.com/documents/612/acm/RT-duroid-6006-6010-laminate-data-sheet.pdf>.